Monthly Notices of the ROYAL ASTRONOMICAL SOCIETY

MNRAS **546,** 1–20 (2026) https://doi.org/10.1093/mnras/stag049
Advance Access publication 2026 January 9

REBELS-IFU: Steeply rising star formation histories and the importance of dust obscuration in massive $z \simeq 7$ galaxies revealed by multiwavelength observations

R. Fisher [1★] R. A. A. Bowler [1] R. K. Cochrane [1] L. E. Rowland [2] M. Stefanon,[3,4] H. S. B. Algera [5] M. Aravena,[6,7] R. Bouwens,[2] E. da Cunha [8,9,10] P. Dayal [11,12,13] A. Ferrara,[14] J. A. Hodge,[2] H. Inami [15] L. Komarova,[3] R. Smit,[16] L. Sommovigo [17] D. P. Stark[18] and P. P. van der Werf[2]

Affiliations are listed at the end of the paper

Accepted 2025 December 29. Received 2025 December 19; in original form 2025 November 10

ABSTRACT

Reliable star formation rate (SFR) measurements are essential for understanding early galaxy evolution, yet derived values rely on several assumptions. To address this problem, we investigate the SFRs of 12 massive ($9 < \log(M_\star/\mathrm{M}_\odot) < 10$) Lyman-break galaxies at $z = 6.5$-7.7, drawn from the Atacama Large Millimeter/submillimeter Array (ALMA) Reionization Era Bright Emission Line Survey (REBELS) program. The multiwavelength data, including *JWST* NIRSpec IFU spectroscopy and ALMA observations, make this a unique sample for investigating SFR tracers at this epoch. We compare SFRs derived from the rest-UV, Hα, and far-infrared emission, and from spectral energy distribution (SED) fits. We apply robust dust attenuation corrections, which are crucial since between 50 and 80 per cent of the star formation is obscured, and find a stellar-to-nebular attenuation ratio of $f = 0.50 \pm 0.08$, consistent with local star-forming galaxies. The majority of the derived total SFRs (medians 25-120 $\mathrm{M}_\odot\mathrm{yr}^{-1}$) place the REBELS galaxies systematically above $z = 7$ literature star-forming main-sequence relations, and our best-fit star formation histories (SFHs) rise more steeply than lower-mass galaxies at the same redshift. We show that these rising SFHs mean commonly used luminosity-to-SFR conversion factors, derived assuming a constant SFH over given time-scales, overestimate the SFRs averaged over these time-scales for our galaxies. We provide updated luminosity-to-SFR calibrations for $z \simeq 7$ galaxies with rising SFHs, showing that commonly assumed rest-UV conversion factors overestimate the 100 Myr average SFR by a factor of $\simeq 3$. Finally, we investigate burstiness indicators in the REBELS-IFU galaxies, finding that the rising SFHs imply that the Hα-to-UV luminosity ratio is an unreliable probe of bursty star formation.

Key words: dust, extinction – galaxies: high-redshift – galaxies: star formation.

1 INTRODUCTION

Measuring the cosmic star formation rate density (SFRD) provides key constraints on the efficiency at which galaxies form stars and evolve throughout the history of the Universe. The SFRD is observed to rise rapidly to a peak around $z \simeq 2$, and decline at later epochs (e.g. P. Madau & M. Dickinson 2014). Underpinning the reliability of SFRD estimates is the derivation of accurate star formation rates (SFRs) for individual galaxies, either from specific features in their observed spectra or from the star formation histories (SFHs) inferred from spectral energy distribution (SED) fits to the observations (for reviews see R. C. Kennicutt 1998; R. C. Kennicutt & N. J. Evans 2012; P. Madau & M. Dickinson 2014). The availability of these features, or 'tracers', depends on observational constraints, such as the wavelength coverage and sensitivity of the imaging or spectroscopic data obtained, in addition to the redshift and intrinsic properties of the galaxy. Since spectral features are not all produced by the same physical processes, obtaining consistent empirical calibrations for each tracer and making galaxy-to-galaxy SFR comparisons is non-trivial, with systematic offsets between SFRs derived via different methods for the same galaxies (e.g. R. Smit et al. 2016; R. K. Cochrane et al. 2021; T. J. Looser et al. 2025; L. Clarke et al. 2024; C. A. Pirie et al. 2025). It also remains unknown whether these calibrations, which are based on local sources, still hold at high redshift, where conditions in galaxies are expected to be more extreme with, for example, harder ionising radiation fields and higher electron densities in the interstellar medium (ISM; e.g. F. Cullen et al. 2016; H. Katz et al. 2022; G. Roberts-Borsani et al. 2024; M. W. Topping et al. 2025a, b).

★ E-mail: rebecca.fisher-7@postgrad.manchester.ac.uk

The empirical calibrations used to obtain SFRs from observed luminosities are derived using stellar population synthesis models (e.g. G. Bruzual & S. Charlot 2003; C. Conroy, J. E. Gunn & M. White 2009). The luminosity-to-SFR conversion rate factor for a given tracer, κ_x, can be calculated for a given stellar initial mass function (IMF), stellar mass range, SFH (usually constant), and stellar population synthesis model. In short, this involves combining stellar templates with a weighting determined by the IMF to create the synthetic spectra of single-age populations as a function of age. With an assumed SFH, a full galaxy SED can then be produced by linearly combining these (for more details see the reviews by R. C. Kennicutt 1998; C. Conroy 2013). Thus, the conversion factors derived from these models, at a minimum, depend on the SFH, galaxy age, metallicity, and IMF, although the relative importance of each factor varies for different tracers and parameter regimes (see P. Madau & M. Dickinson 2014, for details). These models are needed since, while most of the stellar mass in young stellar populations resides in low-mass stars, the massive stars emit the majority of the energy and, thus, most observational tracers probe the formation of massive stars. Different observables are also sensitive to slightly different stellar mass ranges (for example, the stellar mass range probed by the rest-UV extends to lower masses than for Hα; R. C. Kennicutt & N. J. Evans 2012; P. Madau & M. Dickinson 2014). Thus, studying, for example, the SFR-stellar mass relation (the star-forming main-sequence; D. G. York et al. 2000; J. Brinchmann et al. 2004) as a function of redshift requires a careful, consistent combination of different tracers (e.g. K. G. Noeske et al. 2007; K. E. Whitaker et al. 2012; J. S. Speagle et al. 2014; K. E. Whitaker et al. 2014; I. Shivaei et al. 2015; P. Santini et al. 2017; P. Popesso et al. 2022; M. P. Koprowski et al. 2024).

The observations of galaxies at $z > 6$ used to derive SFRs have typically been limited to the rest-UV, with occasional constraints from FIR emission lines (e.g [C II] 158 μm and [O III] 88μm) or continuum from ALMA observations, but the *James Webb Space Telescope* (*JWST*) has now increased the accessibility of rest-optical wavelengths. The rest-UV continuum of young star-forming galaxies in the range 1250-2500 Å is dominated by the light emitted by short-lived ($\lesssim$ 100 Myr), massive (> 3 M$_\odot$) stars (e.g. Z. Huo et al. 2024). The rest-UV luminosity is considered a good indicator of SFR under the assumption that significant fluctuations in the SFR occur over time-scales longer than a few 10s of Myrs and is usually assumed to measure the average SFR over a time-scale of around $\sim$ 100 Myr (C.-N. Hao et al. 2011).

SFRs can also be inferred from rest-optical emission lines, one of the most accessible and reliable of which is Hα (e.g. R. C. Kennicutt 1998; J. Moustakas, J. Robert C. Kennicutt & C. A. Tremonti 2006). Hα emission primarily emanates from the recombination of gas in H II regions that have been photoionised by nearby, massive O stars that have short lifetimes (< 20 Myr; R. C. Kennicutt 1998; R. C. Kennicutt & N. J. Evans 2012; P. Madau & M. Dickinson 2014). Thus, compared to the rest-UV emission, Hα traces a narrower stellar mass range and shorter ($\sim$ 10 Myr) time-scales (e.g. E. J. Murphy et al. 2011; D. R. Weisz et al. 2012; N. Emami et al. 2019; A. L. Faisst et al. 2019; H. Atek et al. 2022). Other lines such as Lyman α, [O II] λ3727, and [O III] λ5007 are also indicators of SFR, but the former is subject to complex radiative transfer effects and the latter two exhibit a complex dependency on the metallicity and excitation state of the ISM (M. Figueira et al. 2022).

One of the key drawbacks of deriving SFRs from the rest-UV or Hα is the impact of dust attenuation. This cannot be ignored, even at high redshift, with studies suggesting that dust-obscured star formation could contribute of order 30 per cent of the total SFRD at $z = 7$ (H. S. B. Algera et al. 2022) and extrapolations suggesting the contribution could be around 20percnt at $z \simeq 8$, and around 5 per cent at $z \simeq 10$ (J. A. Zavala et al. 2021; F.-Y. Liu et al. 2026). Dust attenuation corrections are particularly important in massive galaxies ($\log(M_*/\,\mathrm{M}_\odot) = 8.5$-10), since these tend to have higher metallicities and thus dust content, with studies at $z = 4$-7 finding nearly half of star formation in these massive galaxies to be dust-obscured (e.g. J. S. Dunlop et al. 2017; R. A. A. Bowler et al. 2018; Y. Fudamoto et al. 2021; H. Inami et al. 2022; R. A. A. Bowler et al. 2024; H. S. B. Algera et al. 2024a).

One method to correct dust-attenuated fluxes involves assuming a dust attenuation curve, which describes the attenuation as a function of wavelength. Studies typically assume the attenuation or extinction curves derived from observations of the Milky Way or local galaxies (e.g. J. A. Cardelli, G. C. Clayton & J. S. Mathis 1989; D. Calzetti et al. 2000; K. D. Gordon et al. 2003), or infer the stellar and nebular attenuation curves from the sample of interest (e.g. N. A. Reddy et al. 2015, 2020). An excess in attenuation towards nebular emission lines, known as differential reddening, has been observed in local star-forming galaxies (e.g. M. N. Fanelli, R. W. O'Connell & T. X. Thuan 1988; D. Calzetti 1997b; D. Calzetti et al. 2000; K. Kreckel et al. 2013; Y. Koyama et al. 2019) and also at higher redshift (N. M. F. Schreiber et al. 2009; N. A. Reddy et al. 2010; D. Kashino et al. 2013; S. H. Price et al. 2014; N. A. Reddy et al. 2015, 2020; I. Shivaei et al. 2020; L. Barrufet et al. 2025). This can be explained by a physical picture of ionised gas being located around young, massive stars in birth clouds, which provides a larger dust-covering fraction and/or dust column density, whereas the stellar continuum can originate from a wider variety of stars across the galaxy (e.g. D. Calzetti, A. L. Kinney & T. Storchi-Bergmann 1994; S. Charlot & S. M. Fall 2000). This effect remains a key uncertainty when comparing SFR tracers (e.g. A. L. Faisst et al. 2019). Some studies suggest that the continuum-to-nebular attenuation ratio (see Section 4.2) may evolve from the $f = 0.44$ factor found by D. Calzetti (1997b) to closer to $f = 1$ by $z = 2$ (e.g. D. K. Erb et al. 2006; N. A. Reddy et al. 2010; D. Kashino et al. 2013; Y. Koyama et al. 2015; F. Valentino et al. 2015; A. Puglisi et al. 2016; D. Kashino et al. 2017; A. L. Faisst et al. 2019). The ratio of nebular to continuum attenuation remains poorly constrained at $z > 2$, although measurements are beginning to be made with *JWST* data (e.g. A. Tsujita et al. 2025).

An alternative to correcting the rest-UV or optical emission using a dust attenuation curve is to combine it with an obscured SFR tracer that probes similar time-scales, e.g. the rest-UV and far-infrared (FIR, e.g. R. J. Bouwens et al. 2012; D. Calzetti 2012; M. W. Topping et al. 2022). FIR SFRs are derived from the integrated luminosity between 8 and 1000 μm (R. C. Kennicutt 1998). Dust absorbs the UV radiation from stars and re-emits it at longer wavelengths. Therefore, the FIR luminosity is assumed to be proportional to the obscured SFR. This assumes dust heating from other sources, such as AGN and older stars, is negligible, which is likely a valid assumption at high redshift (P. Madau & M. Dickinson 2014, although see G. T. Jones & E. R. Stanway 2023). The FIR emission is typically modelled as a modified blackbody (MBB), which depends on the physical properties of the dust: the dust temperature (T_d, which determines the wavelength at which the emission peaks), dust mass (M_d), and dust emissivity index

(β_d; e.g. C. M. Casey 2012; L. Sommovigo et al. 2020). The FIR luminosity-to-SFR conversion factor is obtained from models that compute the rest-UV and IR luminosities for various amounts of dust attenuation, with most assuming the foreground dust screen geometry of D. Calzetti et al. (2000), although the exact model used for dust absorption is not thought to be significant (P. Madau & M. Dickinson 2014, although see L. Sommovigo & H. Algera 2025).

In this paper, we study a subsample of galaxies from the Reionization Era Bright Emission Line Survey, known as the REBELS-IFU sample. REBELS-IFU provides a unique dataset for comparing SFR tracers at $z \simeq 7$ since multiwavelength observations extending from the rest-frame UV/optical (*JWST* NIRSpec spectroscopy) to the rest-frame FIR (ALMA) are available (R. J. Bouwens et al. 2022; Stefanon et al., in preparation). This is the only sample of massive ($M_\star > 10^9$ M$_\odot$) galaxies at $z > 6$ that has this wealth of SFR tracers, providing a unique opportunity to investigate the consistency between different methods and shed light on the SFHs of these sources. As *JWST* observations now probe increasingly high redshifts ($z > 9$; e.g. A. J. Bunker et al. 2023; Y. Harikane et al. 2023; R. P. Naidu et al. 2025), where observations are typically limited to the rest-UV since MIRI observations that can recover the rest-optical (e.g. C. Prieto-Jiménez et al. 2025) are less common than NIRSpec observations, it is important to investigate the reliability of rest-UV derived SFRs and the validity of assumptions, such as constant SFHs, in empirical calibrations. From the NIRSpec spectra, we have measurements of key physical properties of these galaxies, including stellar mass (Stefanon et al. in preparation), dust attenuation curves (R. Fisher et al. 2025), and gas-phase metallicities (L. E. Rowland et al. 2025), allowing us to build up a comprehensive picture of these galaxies and reduce the number of assumptions required.

The structure of this paper is as follows: In Section 2, we introduce the REBELS-IFU sample and dataset. In Section 3, we provide details of the methods we use to derive SFRs and apply dust attenuation corrections. We present a detailed investigation of the dust attenuation in our galaxies in Section 4, which is necessary to accurately measure the obscured star formation. Using these dust corrections, we derive SFRs from a range of different tracers in Section 5. We show that our sources have significant dust-obscured star formation fractions and place our galaxies in the context of the star-forming main sequence. We discuss our results in Section 6, explaining discrepancies between SFRs by considering the effects of SFHs and tracer time-scales. We support our findings with simple model SEDs, which we use to investigate the effect of rising SFHs on luminosity-to-SFR conversion factors. Finally, we use our results to discuss the reliability of the Hα-to-UV ratio as a diagnostic of SFH burstiness. The key findings are summarised in Section 7. We assume the standard ΛCDM cosmology with $H_0 = 70$ km s^{-1} Mpc^{-1}, $\Omega_m = 0.3$, and $\Omega_\Lambda = 0.7$ throughout this work (Planck Collaboration VI 2020).

2 DATA AND SAMPLE

The full details of the REBELS-IFU galaxies studied in this work are given in Stefanon et al. (in preparation) and R. Fisher et al. (2025). In short, these galaxies are a subsample of the 40 rest-UV bright ($M_{UV} < -21$) Lyman-break galaxies at $z = 6.5$-8 with stellar masses $\log_{10}(M_*/\,\mathrm{M}_\odot) = 8.8 - 10.4$ targeted by the REBELS ALMA large program (R. J. Bouwens et al. 2022). Twelve galaxies with bright [C II] 158 μm emission in the REBELS program were selected for follow-up with *JWST* NIRSpec observations (PID 1626; P.I. Stefanon and PID 2659; P.I. Weaver, *JWST* Cycle 1). These sources are listed in Table 1. The physical properties of these galaxies are representative of the full REBELS sample (see Stefanon et al. in preparation), but their SFRs inferred in previous work, for example from [C II] of 50-400 M$_\odot$yr^{-1}, are significantly higher than typical galaxies at these redshifts (I. De Looze et al. 2014). The SFRs inferred from the rest-UV and FIR emission of the REBELS galaxies tend to be lower than those inferred from [C II] (A. Ferrara et al. 2022; L. Sommovigo et al. 2022a; R. A. A. Bowler et al. 2024), but still tend to place the REBELS sources systematically above literature star-forming main-sequence relations, which is unsurprising given their bright rest-UV selection. However, the magnitude of the offset from the star-forming main-sequence depends strongly on the method used to derive stellar mass (H. S. B. Algera et al. 2022; M. W. Topping et al. 2022).

The NIRSpec integral field unit (IFU) observations probe the rest-UV and rest-optical wavelengths of the galaxies. These observations use the PRISM/CLEAR disperser-filter combination with a resolution of $R \simeq 100$, and an exposure time of approximately 30 min per source. For each 0.08 arcsec spaxel in the 3.1 arcsec × 3.2 arcsec field of view, a spectrum covering the wavelength range 0.6-5.3 μm is obtained. In this work, we study the global properties of the galaxies derived from the integrated spectra (see Stefanon et al. in preparation and L. E. Rowland et al. 2025, for details). The full details of the cube data reduction are presented in Stefanon et al. (in preparation), and we use the emission-line flux measurements presented in L. E. Rowland et al. (2025).

ALMA Band 6 or Band 7 observations of these sources were obtained as part of the Cycle 7 REBELS ALMA large programme (PID: 2019.1.01634.L, P.I. Bouwens). The dust continuum emission is simultaneously observed during the spectral scans searching for the [C II]158 μm or [O III] 88 μm lines. All twelve of the REBELS-IFU galaxies were spectroscopically confirmed via the detection of their [C II] 158 μm line (R. J. Bouwens et al. 2022). Dust continuum emission was also detected with a signal-to-noise ratio of $\geq 3.5\sigma$ for ten of the twelve REBELS-IFU galaxies (see Table 1 and H. Inami et al. 2022). Published multiband ALMA observations are available for three sources and are used for the two sources where these provide useful constraints on the FIR SED (e.g. H. S. B. Algera et al. 2024a, b). Improved constraints on the remaining sources will soon be possible thanks to recent Band 8 observations (PID: 2024.1.00406.S, P.I. Algera).

3 METHODS

An illustration of the available data and the different methods that we use to infer SFRs is shown in Fig. 1. We show an observed NIRSpec rest-UV/optical spectrum for one of our galaxies. The difference between this spectrum and the reconstructed intrinsic SED (dashed line) demonstrates the wavelength-dependent impact of dust attenuation on our SFR tracers, with the rest-UV being more attenuated than Hα. We will also make use of the non-parametric SFHs from the SED fits with a flexible dust attenuation curve to the full NIRSpec spectra presented in R. Fisher et al. (2025). In the right panel, we show a modified blackbody curve and the FIR ALMA dust continuum detection. The shaded area under this curve is used to measure the dust-obscured SFR.

Table 1. The 12 REBELS galaxies targeted with the NIRSpec IFU observations used in this study. Column (1): Galaxy identifier. Column (2): Spectroscopic redshift from the [C II] detection from ALMA with a typical uncertainty of $\Delta z \simeq 0.0002$ (R. J. Bouwens et al. 2022). Column (3): Rest-frame UV-continuum slope, $\beta_{\rm UV}$, from R. Fisher et al. (2025). Column (4): Balmer decrement, H α/H β, derived from the emission-line fluxes from L. E. Rowland et al. (2025) for the galaxies at $6.5 \leq z < 7.0$ for which H α lies within the NIRSpec wavelength coverage. Column (5): Stellar mass, $M_\star$, from the BAGPIPES SED fits with a flexible dust attenuation curve (R. Fisher et al. 2025). Note that these differ from those presented in Stefanon et al. (in preparation), who assume a fixed Calzetti dust attenuation curve, but are consistent within the errors. Column (6): Gas-phase metallicities, $Z_{\rm gas}$, derived from optical emission lines (L. E. Rowland et al. 2025). Column (7): Colour excess for the ionised gas (nebular regions) derived using the Balmer decrement and equation (4), assuming the attenuation curves of R. Fisher et al. (2025). Column (8): Colour excess for the stellar continuum calculated using equation (5). Column (9): Infrared-excess, IRX, using $L_{\rm IR}$ values from R. A. A. Bowler et al. (2024), which assume a fixed dust temperature of $T_{\rm d} = 46$ K and emissivity index $\beta_{\rm d} = 2.0$, except for REBELS-25 and REBELS-38 (marked with *) for which we use the $L_{\rm IR}$ values derived from multiband ALMA data (H. S. B. Algera et al. 2024a, b).

ID (1)	z (2)	$\beta_{\rm UV}$ (3)	Hα/Hβ (4)	$\log(M_*/{\rm M}_\odot)$ (5)	$12+\log({\rm O/H})$ (6)	$E(B-V)_{\rm gas}$ (7)	$E(B-V)_{\rm stellar}$ (8)	IRX (9)
REBELS-05	6.496	-1.42 ± 0.06	3.76 ± 0.45	$9.60^{+0.10}_{-0.10}$	8.51 ± 0.16	0.24 ± 0.11	$0.11^{+0.03}_{-0.03}$	0.58 ± 0.09
REBELS-08	6.749	-1.92 ± 0.05	4.05 ± 0.60	$9.31^{+0.10}_{-0.10}$	8.22 ± 0.20	0.30 ± 0.13	$0.08^{+0.02}_{-0.02}$	0.59 ± 0.09
REBELS-12	7.346	-1.67 ± 0.03	–	$9.80^{+0.09}_{-0.09}$	8.23 ± 0.13	–	$0.06^{+0.03}_{-0.03}$	0.39 ± 0.12
REBELS-14	7.084	-1.74 ± 0.03	–	$9.54^{+0.14}_{-0.12}$	7.90 ± 0.12	–	$0.06^{+0.03}_{-0.02}$	0.23 ± 0.10
REBELS-15	6.875	-2.01 ± 0.03	3.48 ± 0.33	$9.40^{+0.03}_{-0.03}$	7.78 ± 0.30	0.17 ± 0.08	$0.09^{+0.02}_{-0.02}$	< 0.22
REBELS-18	7.675	-1.56 ± 0.03	–	$9.98^{+0.04}_{-0.04}$	8.50 ± 0.13	–	$0.10^{+0.02}_{-0.02}$	0.42 ± 0.08
REBELS-25	7.307	-1.61 ± 0.09	–	$9.07^{+0.08}_{-0.10}$	8.62 ± 0.17	–	$0.09^{+0.03}_{-0.02}$	$0.79^{+0.30*}_{-0.20}$
REBELS-29	6.685	-1.89 ± 0.05	3.16 ± 0.37	$9.94^{+0.08}_{-0.06}$	8.73 ± 0.15	0.09 ± 0.10	$0.09^{+0.03}_{-0.02}$	0.32 ± 0.10
REBELS-32	6.729	-1.34 ± 0.07	3.48 ± 0.36	$9.75^{+0.13}_{-0.11}$	8.48 ± 0.13	0.17 ± 0.09	$0.12^{+0.04}_{-0.04}$	0.67 ± 0.13
REBELS-34	6.634	-2.23 ± 0.03	3.89 ± 0.84	$9.59^{+0.08}_{-0.09}$	8.33 ± 0.29	0.27 ± 0.20	$0.03^{+0.02}_{-0.01}$	< 0.32
REBELS-38	6.577	-1.63 ± 0.06	3.98 ± 0.54	$9.93^{+0.09}_{-0.08}$	8.28 ± 0.18	0.28 ± 0.12	$0.13^{+0.03}_{-0.03}$	$0.24^{+0.23*}_{-0.17}$
REBELS-39	6.845	-2.07 ± 0.04	3.43 ± 0.40	$9.57^{+0.10}_{-0.11}$	8.02 ± 0.29	0.16 ± 0.10	$0.05^{+0.02}_{-0.01}$	0.30 ± 0.09

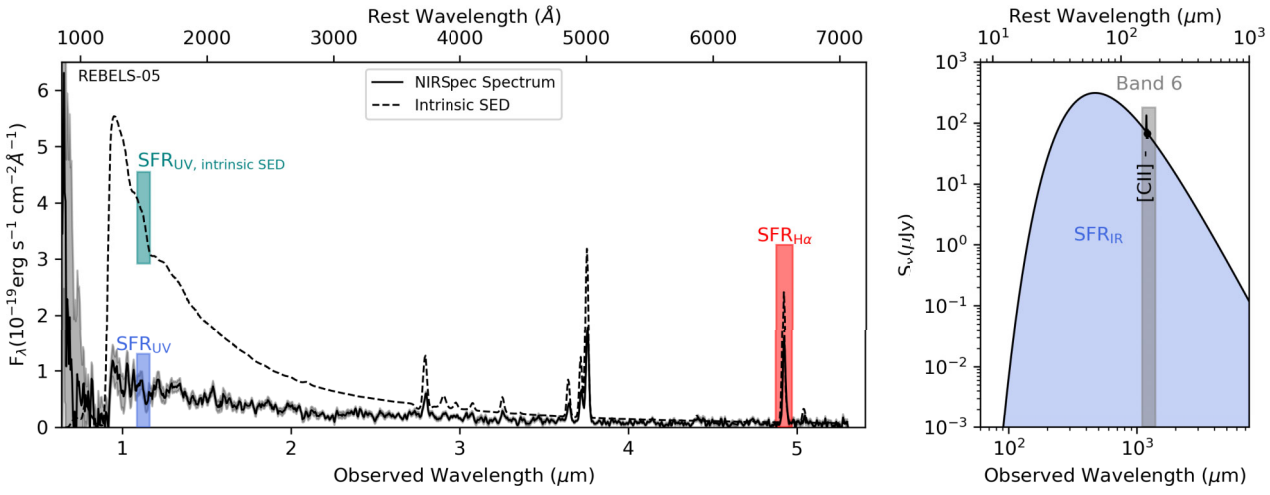

Figure 1. We show with coloured rectangles the wavelength ranges used to infer SFRs in this work. The full NIRSpec PRISM spectrum for one of the REBELS-IFU galaxies (REBELS-05) is shown by the solid black line in the left panel. The intrinsic, dust-free SED model is shown by the dashed line, demonstrating the wavelength-dependent effect of dust attenuation, with the rest-UV flux being impacted more than the H α flux. The right panel shows a modified blackbody model of the rest-frame far-infrared emission. The ALMA Band 6 flux continuum measurement is shown by the black point. The integrated flux under this curve traces the dust-obscured SFR.

3.1 Deriving SFRs from the rest-UV, Hα, and FIR luminosities

The conversion factors, $\kappa_{\rm x}$, we use in equations of the form ${\rm SFR_x} = \kappa_{\rm x} L_{\rm x}$ to obtain SFRs from the luminosities, $L_{\rm x}$, of each tracer are given in Table 2. For our fiducial values, we adopt those which are used extensively in the literature; however, we will discuss the effects of different metallicities and SFHs on these values in Section 6.4. We adjust all the conversion factors to the G. Chabrier (2003) IMF with stellar population mass limits of 0.1-100 ${\rm M}_\odot$ using the 0.63 factor given in P. Madau & M. Dickinson (2014). For consistentcy with previous analysis of the REBELS sources (e.g. H. S. B. Algera et al. 2022; R. J. Bouwens et al. 2022; R. A. A. Bowler et al. 2024), we adopt the standard conversion factors from P. Madau & M. Dickinson (2014) for $\kappa_{\rm UV}$ and $\kappa_{\rm IR}$, which assume a constant SFR during the previous 100 Myr and a fixed stellar metallicity of $Z_* = 0.1\ {\rm Z}_\odot$. The observed rest-

Table 2. The calibrations we assumed to convert luminosities to SFRs for each tracer.

SFR_x	=	$\kappa_x L_x$	Source
SFR_{UV}	=	$7.2 \times 10^{-29} L_\nu$ [erg s^{-1} Hz^{-1}]	P. Madau & M. Dickinson (2014) adjusted for G. Chabrier (2003) IMF ($1.15 \times 10^{-28} \times 0.63$)
SFR_{IR}	=	$1.1 \times 10^{-10} L_{IR}$ [$L_\odot$]	P. Madau & M. Dickinson (2014) adjusted for G. Chabrier (2003) IMF ($1.73 \times 10^{-10} \times 0.63$)
$SFR_{H\alpha}$	=	$4.977 \times 10^{-42} L_{H\alpha}$ [erg s^{-1}]	R. C. Kennicutt (1998) adjusted for G. Chabrier (2003) IMF ($7.9 \times 10^{-42} \times 0.63$)

UV luminosity, L_{UV}, was calculated from the spectrum flux, F_λ, in a top hat filter of width 100 Å centred at $\lambda_{rest} = 1500$ Å. We use the rest-frame FIR luminosity values, L_{IR}, from R. A. A. Bowler et al. (2024), which assume a dust temperature of $T_d = 46$ K and a dust emissivity index of $\beta_d = 2.0$, except for REBELS-25 and REBELS-38 for which we use the values derived by H. S. B. Algera et al. (2024b) and H. S. B. Algera et al. (2024a), respectively, that use the multiband ALMA observations available for these sources. This choice of T_d is justified based on the [C II]-based method of L. Sommovigo et al. (2022a), and is consistent with the values obtained from the modified blackbody fits to multiband ALMA observations (H. S. B. Algera et al. 2024a). We do not use the L_{IR} derived by H. S. B. Algera et al. (2024a) for REBELS-12 since it is undetected in the Band 8 data and thus, the constraints on the FIR SED are poor. For $SFR_{H\alpha}$, we use the conversion factor from R. C. Kennicutt (1998) which assumes an electron temperature of $T_e = 10^4$ K, solar stellar metallicity, Case B recombination, and a constant SFR for at least 10 Myr. We take the H α emission-line fluxes measured directly from the observed NIRSpec spectra from L. E. Rowland et al. (2025).

Here, we summarise some of the caveats and assumptions associated with these conversion factors, which will be discussed in more detail in Section 6.3. We note that each κ value assumes a fixed stellar metallicity, whereas the gas-phase metallicities of our sample are known to vary between $Z_{gas} = 0.12$-$1.11\ Z_\odot$ (although these are not necessarily equal to the stellar metallicities; L. E. Rowland et al. 2025). $\kappa_{H\alpha}$ is more sensitive to metallicity than κ_{UV}, but our main conclusions remain unchanged even if we adopt other commonly used conversion factors or account for this variability.

As shown in Fig. 1, both the rest-frame UV and H α emission are attenuated by dust. To obtain total SFRs that include the contributions from dust-obscured star formation, an attenuated tracer can be combined with one that measures the obscured SFR over the same time-scale, e.g. combining SFR_{UV} and SFR_{IR}. Alternatively, the total SFR can be obtained by applying a dust correction to convert the observed flux, f_{obs}, to the intrinsic flux, f_{int}, using

$$f_{int}(\lambda) = f_{obs}(\lambda) 10^{0.4 A(\lambda)}, \tag{1}$$

where $A(\lambda)$ is the attenuation magnitude at that wavelength. To correct the rest-UV (H α) SFRs thus requires assuming a stellar (nebular) dust attenuation curve for each galaxy. We summarise our dust attenuation correction methods in the following subsection.

3.2 Correcting SFRs with dust attenuation curves

The total dust attenuation curve, $k(\lambda)$, that describes the wavelength-dependent effect of dust absorption and scattering of stellar photons, is related to the attenuation magnitude, $A(\lambda)$, at wavelength λ by

$$k(\lambda) = \frac{A(\lambda)}{E(B-V)}, \tag{2}$$

where $E(B-V)$ is known as the colour excess. The colour excess is the difference between the B-band (4400 Å) attenuation magnitude, A_B, and the V band (5500 Å) attenuation magnitude, A_V. This is related to the total-to-selective extinction ratio, R_V, by

$$E(B-V) = A_B - A_V = \frac{A_V}{R_V}. \tag{3}$$

The colour excess of the ionised gas in a galaxy, $E(B-V)_{gas}$, can be calculated from the flux ratio of the hydrogen Balmer lines (the Balmer decrement) using

$$E(B-V)_{gas} = \frac{2.5 \log\left(\frac{(H\alpha/H\beta)_{obs}}{(H\alpha/H\beta)_{int}}\right)}{k(\lambda_{H\beta}) - k(\lambda_{H\alpha})}, \tag{4}$$

where $(H\alpha/H\beta)_{obs}$ is the observed flux ratio and $(H\alpha/H\beta)_{int}$ is the intrinsic ratio. We assume Case B recombination with intrinsic ratios of $H\alpha : H\beta : H\gamma = 2.86 : 1.0 : 0.47$ for a temperature of 10^4 K and electron density $n_e = 100$ cm^{-3} (J. S. Miller 1974). It has been shown that this intrinsic ratio does not significantly vary for the range of physical conditions expected in regions of star formation, with the Balmer decrement changing by less than 10 per cent for variations in gas temperature between 5000-20 000 K and electron density 100-10 000 cm^{-3} (D. Osterbrock & G. J. Ferland 2006; A. Smith et al. 2022; L. Sandles et al. 2024), although we note that anomalous ratios inconsistent with Case B recombination have recently been observed at high redshift (e.g. H. Yanagisawa et al. 2024). For the four REBELS-IFU galaxies at $z > 7$ (REBELS-12, REBELS-14, REBELS-18, and REBELS-25), H α is redshifted beyond the wavelength range of NIRSpec. Since H γ is blended with [O III]λ4363+[Fe II] λ4360 in the low-resolution prism spectra, we can only obtain a lower limit on the $H\beta/H\gamma$ ratio and thus cannot accurately dust correct the $SFR_{H\alpha}$ values (inferred from the Hβ flux) for four of the REBELS-IFU galaxies (for a detailed discussion see L. E. Rowland et al. 2025).

The colour excess of the stellar continuum, $E(B-V)_{stellar}$, is calculated using

$$E(B-V)_{stellar} = \frac{A_{V,stellar}}{R_V}, \tag{5}$$

where $A_{V,stellar}$ and R_V are obtained from the SED fits with a flexible dust attenuation curve presented in R. Fisher et al. (2025). For the S. Salim, M. Boquien & J. C. Lee (2018), power-law parametrisation of the dust attenuation curve slope, R_V is calculated using

$$R_V = \frac{R_{V,Calzetti}}{(R_{V,Calzetti} + 1)(4400/5500)^\delta - R_{V,Calzetti}}, \tag{6}$$

where $R_{V,Calzetti} = 4.05$ and δ is the deviation of the attenuation curve slope from the Calzetti-like curve.

3.3 Correcting SFRs with the IRX–β_{UV} relation

The FIR-to-rest-UV luminosity ratio, known as the infrared-excess, $IRX = \log_{10}(L_{IR}/L_{UV})$, is a proxy for the obscured-to-unobscured SFR ratio. Under the assumption of energy balance, the relation between this and the rest-frame UV slope, β_{UV}, (the

IRX–$\beta_{\rm UV}$ relation) provides indirect constraints on dust attenuation curves since $L_{\rm IR}$ is proportional to $M_{\rm d}$, whereas $\beta_{\rm UV}$ depends on the dust column density of the ISM along the line of sight to the observer. For the IRX–$\beta_{\rm UV}$ relation, we adopt the equation

$$\mathrm{IRX} = \log_{10}\left(1.71 \times \left(10^{0.4A(1600)} - 1\right)\right) \quad (7)$$

from R. J. McLure et al. (2018). Under the assumption that the intrinsic UV-slopes, $\beta_{\rm UV,0}$, of star-forming galaxies are similar, we can use the relation

$$A(1600) = \frac{\mathrm{d}A_{1600}}{\mathrm{d}\beta_{\rm UV}}(\beta_{\rm UV} - \beta_{\rm UV,0}), \quad (8)$$

where $\mathrm{d}A_{1600}/\mathrm{d}\beta_{\rm UV}$ is the slope of the dust attenuation curve. For reference, for the D. Calzetti et al. (2000) dust attenuation curve $\mathrm{d}A_{1600}/\mathrm{d}\beta_{\rm UV} = 1.97$, while for the SMC extinction (K. D. Gordon et al. 2003) $\mathrm{d}A_{1600}/\mathrm{d}\beta_{\rm UV} = 0.91$. We measure the rest-frame UV-slope, $\beta_{\rm UV}$, directly from the observed spectra by fitting a power-law between the rest-frame wavelengths $\lambda_{\rm rest} = 1268 - 2580$ Å using a least-squares fitting method. These values are consistent within the errors with fits where we mask the spectral regions given in A. Saxena et al. (2024) that could include contributions from broadened rest-UV lines. This suggests there are no strong emission or absorption features in the rest-UV region. The relation

$$M_{\rm UV} = -2.5\log(L_{\rm UV}) + 5.814 \quad (9)$$

was used to convert from the monochromatic rest-frame UV magnitude, $M_{\rm UV}$, to $L_{\rm UV}$ in units of $\mathrm{L}_{\odot}$ (P. L. Capak et al. 2015). Equation (7) can be fitted to data if rest-frame FIR observations are available, providing an indirect constraint on the average dust attenuation curve. Alternatively, by assuming a dust attenuation curve and an intrinsic UV-slope, the obscured SFR of a galaxy can be inferred via the IRX, which is a proxy for $\mathrm{SFR_{IR}/SFR_{UV}}$.

4 STELLAR AND NEBULAR DUST ATTENUATION CORRECTIONS

In the following section, we present a detailed investigation of dust attenuation in our sources, which is necessary to accurately measure the contribution of dust-obscured star formation.

4.1 The Balmer decrement

To measure the nebular dust attenuation and obtain dust-corrected Hα SFRs, we use the Balmer decrement, $\mathrm{H}\,\alpha/\mathrm{H}\,\beta$. In Fig. 2, we plot H$\alpha$/H$\beta$ against stellar mass for the eight REBELS-IFU galaxies at $6.5 \leq z < 7.0$ for which $\mathrm{H}\,\alpha$ lies within the NIRSpec wavelength coverage. The deviation of this ratio from the intrinsic value for Case B recombination of 2.86 depends on the total mass of dust present and its spatial distribution in the galaxy. All of the REBELS-IFU $\mathrm{H}\alpha/\mathrm{H}\,\beta$ ratios exceed this intrinsic value, consistent with this nebular emission being dust attenuated.

The REBELS-IFU galaxies are consistent with the positions of local, rest-optically selected SDSS galaxies with similar stellar masses, shown by the greyscale histogram (R. Ahumada et al. 2020). This suggests that the dust properties of our sample, specifically the dust-mass surface density to stellar mass ratio (A. E. Shapley et al. 2023), are not significantly different to local sources. We also show the results of A. J. Battisti et al. (2022) derived from *HST* grism observations of galaxies at $0.75 < z < 1.5$. For comparison, we show the JADES galaxies in the same redshift range as our sample (D. J. Eisenstein et al. 2025;

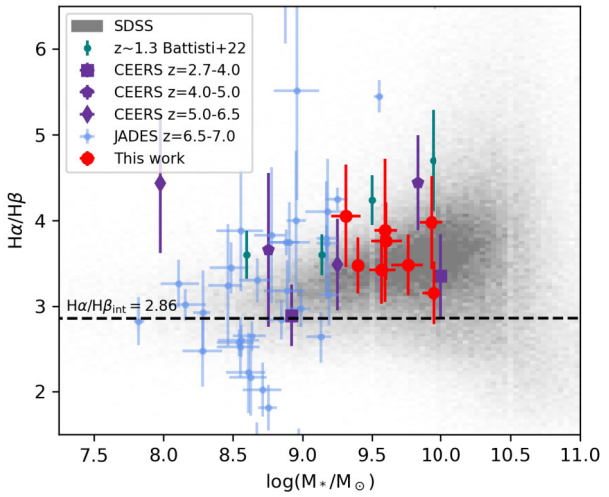

Figure 2. The Balmer decrements, $\mathrm{H}\,\alpha/\mathrm{H}\beta$, are plotted against stellar mass, $M_\star$, in red for the 8 of the 12 massive REBELS-IFU galaxies at $6.5 \leq z < 7.0$ for which $\mathrm{H}\,\alpha$ lies within the NIRSpec wavelength coverage. The $\mathrm{H}\,\alpha/\mathrm{H}\beta$ ratios all exceed the intrinsic Case B recombination value of 2.86, shown by the horizontal dashed line, indicative of dust attenuation affecting the nebular emission of these galaxies. In teal we show the results based on *HST* grism data from A. J. Battisti et al. (2022) at $0.75 < z < 1.5$. The results from stacked CEERS galaxy spectra (A. E. Shapley et al. 2023) are shown in purple, and JADES galaxies at the same redshift as the REBELS-IFU sample are shown in blue. The REBELS-IFU galaxies are consistent with local galaxies of similar stellar masses from the SDSS survey, shown by the grey histogram, suggesting no significant evolution in the Balmer decrement against stellar mass relation with redshift.

A. J. Bunker et al. 2024; F. D'Eugenio et al. 2025) and results from the *JWST* CEERS Survey using NIRSpec Micro-Shutter Assembly (MSA) stacked spectroscopy from A. E. Shapley et al. (2023) spanning $z = 2.7$-6.5. The REBELS-IFU galaxies lie at the higher redshift end of the sample from A. E. Shapley et al. (2023) and the higher stellar mass end of the JADES galaxies at the same redshifts. The Hα/Hβ ratios are consistent with galaxies of similar stellar masses across the full redshift range, supporting the findings of other studies that suggest that the Balmer decrement against stellar mass relation does not significantly evolve with redshift (e.g. A. E. Shapley et al. 2023; C. Woodrum et al. 2025). However, we urge caution in the interpretation of this result since, as discussed in Section 5.3 of A. J. Battisti et al. (2022), the stellar mass and Balmer decrement values in the literature are not always derived from the same apertures. For example, the SDSS stellar masses derived from the same fibre-regions that the Balmer decrements are measured from are approximately 0.5 dex lower than the total stellar mass we plot in Fig. 2. The use of consistent apertures matters when galaxies exhibit Balmer decrement gradients, typically with larger values in central regions compared to the outskirts. These gradients may also be present at higher redshifts (e.g. S. Fujimoto et al. 2025).

4.2 Differential dust attenuation is still important at z ≃ 7

In Fig. 3, we compare the colour excess determined from the ionised gas (nebular regions) derived from Hα/Hβ (equation 4) to those for the stellar continuum (equation 5). In most cases, the colour excess of the ionised gas exceeds that

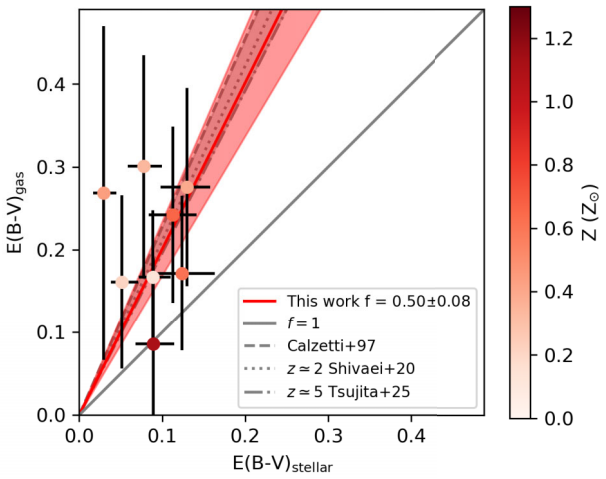

Figure 3. The colour excess measured for the ionised gas, $E(B-V)_{\rm gas}$, derived from the Balmer decrement, compared to the colour excess measured for the stellar continuum, $E(B-V)_{\rm stellar} = A_{V,\rm stellar}/R_V$, for the 8 of the 12 massive galaxies in the REBELS-IFU sample at $6.5 \leq z < 7.0$ for which Hα lies within the NIRSpec wavelength coverage. The average stellar-to-nebular attenuation ratio of $f = (0.50 \pm 0.08)$ is shown by the red line, indicating on average the nebular regions in these galaxies are approximately 2 times more dust-obscured than the stellar continuum. This is consistent with the $f = 0.44$ relation (dashed line) derived for local star-forming galaxies by D. Calzetti (1997a), and the relations for the ALPINE galaxies at $z \simeq 5$ (A. Tsujita et al. 2025) and the MOSDEF galaxies at $z \simeq 2$ (I. Shivaei et al. 2020), shown by the dash–dotted and dotted lines, respectively. The points are coloured by their gas-phase metallicities (L. E. Rowland et al. 2025).

measured for the stellar continuum. The linear fit to the eight REBELS-IFU galaxies for which Hα lies within the NIRSpec wavelength coverage gives a stellar-to-nebular attenuation ratio $f = E(B-V)_{\rm stellar}/E(B-V)_{\rm gas} = 0.50 \pm 0.08$. This is consistent, within the errors, with the $f = 0.44$ factor derived by D. Calzetti (1997a) for local star-forming galaxies. This value also shows good agreement with the value of $f = 0.51^{+0.04}_{-0.03}$ derived for the main-sequence ALPINE galaxies at $z \simeq 5$ (A. L. Faisst et al. 2026; A. Tsujita et al. 2025) and the relation seen in star-forming galaxies at $z = 1.4 - 2.6$ by I. Shivaei et al. (2020). Thus, we see no clear evolution in the ratio with redshift (in contrast to recent results from the JADES survey; C. Woodrum et al. 2025). However, we note that there is a large degree of scatter around this relation for individual galaxies, as has also been seen in other studies (e.g. N. A. Reddy et al. 2015; R. L. Theios et al. 2019; N. A. Reddy et al. 2020; I. Shivaei et al. 2020; H. Atek et al. 2022), and that the errors on individual f values remain large even with our strong detections of the Balmer lines. While our average relation is consistent with the commonly assumed $f = 0.44$ factor, we caution that for individual galaxies, inferring the nebular attenuation from the continuum attenuation using this linear relation is unreliable since f ranges between 0.1 and 1 in our sample (with a standard deviation of 0.27). This justifies our decision to exclude from our analysis the $\rm SFR_{H\alpha}$ values for galaxies in the REBELS-IFU sample for which we cannot measure the Balmer decrement.

One of the key strengths of our comparison is that we use the stellar attenuation curve derived for each galaxy in R. Fisher et al. (2025). However, we note that it is often assumed that the nebular and stellar attenuation curves are different, with the J. A. Cardelli et al. (1989) curve often assumed for the nebular regions. Using a sample of the MOSDEF galaxies, N. A. Reddy et al. (2020) measured the nebular attenuation curve at $z \simeq 2$ and did indeed find a relation close to the J. A. Cardelli et al. (1989) Galactic extinction curve at rest-optical wavelengths. In local SDSS galaxies, S. Rezaee et al. (2021) finds the nebular attenuation curve has a near-universal shape, similar in both shape and normalisation to the Galactic (J. A. Cardelli et al. 1989), SMC (K. D. Gordon et al. 2003), and MOSDEF results at $z \simeq 2$ (N. A. Reddy et al. 2020) within 2σ, 2σ, and 1σ, respectively. However, the nebular attenuation curve measured for a galaxy at $z = 4.41$ deviates significantly from local templates (R. L. Sanders et al. 2025). Unfortunately, we are unable to place strong constraints on the nebular attenuation curve for our galaxies by comparing multiple Balmer line ratios, since in our PRISM spectra Hγ is blended with other emission lines and the signal-to-noise (S/N) ratios of higher-order Balmer emission lines are too low. Thus, the nebular attenuation curve remains a key uncertainty at high redshift. We find very tentative suggestions of deviations from standard curves at shorter wavelengths when using a stack of the spectra, but investigating this further in our sample requires higher resolution spectroscopy to deblend the Balmer lines, with sufficient depth to enable high S/N measurements of the higher-order lines. In Appendix A, we explore the impact of different assumptions about nebular and stellar attenuation curves on the inferred f values. The inferred f varies slightly with different assumptions (e.g. $f = (0.50 \pm 0.08)$ for our fiducial set-up, compared to $f = (0.42 \pm 0.07)$ when assuming a Cardelli extinction curve for the nebular component, and $f = (0.56 \pm 0.10)$ when assuming a Calzetti curve for both nebular and stellar components). However, these values are formally consistent at the 1-sigma level. Thus, our assumption throughout this paper that the dust attenuation curves derived in R. Fisher et al. (2025) apply to both the ionised gas and stellar continuum does not significantly affect our conclusions.

We find tentative suggestions of a correlation between the ratio of the gas-to-stellar attenuation and the gas-phase metallicity, with the most metal-rich galaxy (REBELS-29) lying on the 1-to-1 relation. However, we caution that the correlation is not statistically significant and there are large error bars on $E(B-V)_{\rm gas}$. A trend between this ratio and metallicity has been seen at $z \simeq 2$ in the MOSDEF galaxies and is consistent with the findings of other studies (see I. Shivaei et al. 2020, and references therein). This can be explained physically if in high-metallicity galaxies there is a high surface density of dusty clouds that affect both the ionised gas and stellar continuum, whereas in lower metallicity galaxies there are two distinct dust components: the diffuse ISM dust and dusty birth clouds. M. Pannella et al. (2015) suggest that galaxies with high star formation surface densities and larger dust-to-gas (DtG) ratios have dense ISMs, which reddens the stellar continuum to a similar degree as the nebular emission. If our galaxies followed the A. Rémy-Ruyer et al. (2014) local relation of increasing DtG ratios with metallicity, this would support this interpretation (see H. Algera et al. 2026).

4.3 The IRX–$\beta_{\rm UV}$ relation

ALMA observations of the rest-frame FIR emission provide measurements of the infrared luminosity, a proxy for the dust-obscured SFR. In Fig. 4, we show the IRX–$\beta_{\rm UV}$ relation using the $\beta_{\rm UV}$ and $L_{\rm UV}$ values obtained from the NIRSpec spectra in combination with $L_{\rm IR}$ values derived by R. A. A. Bowler et al. (2024), which assume $T_{\rm d} = 46$ K and $\beta_{\rm d} = 2.0$. We also show the

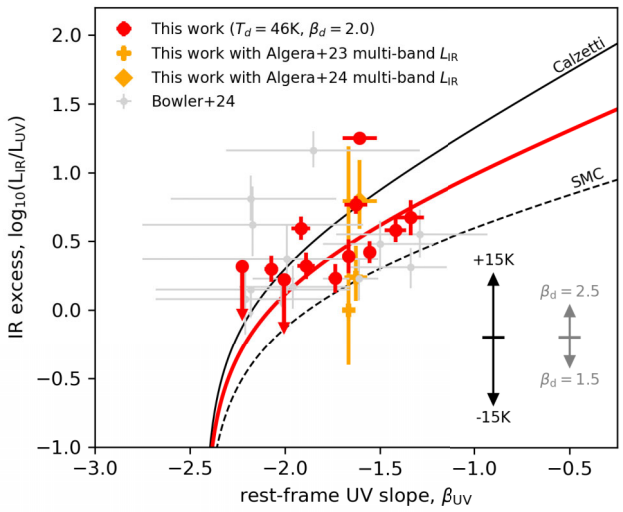

Figure 4. The IRX–β_{UV} points for the 12 REBELS-IFU galaxies at $z \simeq 7$. The rest-frame UV continuum slope, β_{UV}, and luminosity, L_{UV}, values are measured directly from the NIRSpec spectra. In red, we show the points using L_{IR} derived by R. A. A. Bowler et al. (2024), which assume $T_d = 46$ K and $\beta_d = 2.0$, but with rest-UV quantities re-derived from the NIRSpec spectra. The arrows in the bottom right show the median systematic shifts in these IRX values for variations in T_d and β_d. The orange points use the L_{IR} values of H. S. B. Algera et al. (2024a) and H. S. B. Algera et al. (2024b) derived from multiband ALMA observations. The red line shows the best-fit IRX–β_{UV} relation with the intrinsic rest-UV slope fixed to the median value from R. Fisher et al. (2025): $\beta_{UV,0} = -2.43$. This lies between the expected relations for the Calzetti-like attenuation and SMC extinction curves, shown by the solid and dashed black lines, respectively.

values using L_{IR} derived from multiband ALMA data where these are available (H. S. B. Algera et al. 2024a, b). These have larger errors since the modified blackbody fits do not assume a fixed dust temperature and thus have more free parameters. The errors on the rest-UV slope and L_{UV} are significantly reduced compared to the photometrically derived values from R. A. A. Bowler et al. (2024). The scatter in β_{UV} values is also significantly reduced.

The IRX–β_{UV} points shown in Fig. 4 mostly lie between the D. Calzetti et al. (2000) starburst relation and the SMC extinction curve. We fit the data points of the dust continuum-detected galaxies, replacing the L_{IR} values for REBELS-25 and REBELS-38 with those presented in H. S. B. Algera et al. (2024b) and H. S. B. Algera et al. (2024a), respectively, since these are well-constrained by multiband ALMA observations. We fix $\beta_{UV,0} = -2.43$; the median intrinsic UV-slope from the SED models of R. Fisher et al. (2025) and obtain $dA_{1600}/d\beta_{UV} = 1.44 \pm 0.14$. The fit is consistent with the average attenuation curve slope found in R. Fisher et al. (2025), which is slightly steeper than the D. Calzetti et al. (2000) attenuation curve. This result is also consistent with the value obtained by R. A. A. Bowler et al. (2024) using the full REBELS sample of $dA_{1600}/d\beta_{UV} = 1.38 \pm 0.09$ when assuming $\beta_{UV,0} = -2.5$.

We note the usual caveats of assuming a fixed dust temperature, T_d, when calculating L_{IR}. In addition to the average evolution towards higher dust temperatures with increasing redshift (e.g. L. Sommovigo et al. 2022a; G. T. Jones & E. R. Stanway 2023), dust temperatures are also observed to vary between galaxies (e.g. H. S. B. Algera et al. 2024a, b). With a fixed dust emissivity index, a change of temperature of 10 K can shift IRX values by 0.4 dex (I. Mitsuhashi et al. 2024; R. A. A. Bowler et al. 2024). For most of our sample, only a single ALMA band detection is available to constrain the modified blackbody SED fit to the rest-frame FIR continuum (although recently obtained observations will increase this to two in the future; Algera et al., in preparation). The source with the best-constrained FIR SED in our sample, REBELS-25, has been observed in six ALMA bands (5 detections, 1 limit), and the FIR SED fit has yielded a $T_d = 32^{+9}_{-7}$ and $\beta_d = 2.5 \pm 0.4$ (H. S. B. Algera et al. 2024b). As shown in Fig. 4, this causes a downwards vertical shift in the position of this galaxy compared to assuming $T_d = 46$ K. The calculation of L_{IR} also depends on the assumption of the dust emissivity index value, β_d, which has been observed to vary at high redshift. While the results from galaxies between $4 < z < 8$ by J. Witstok et al. (2023) suggest a value of $\beta_d = 1.8 \pm 0.3$, we note that other studies have found values outside of this range (e.g. G. J. Bendo et al. 2025). With a fixed dust temperature, a change in β_d of 0.5 can shift our IRX values by 0.2 dex. Since we cannot place further constraints on these parameters without the analysis of the multiband ALMA observations, we indicate in Fig. 4 the median systematic shifts in IRX when independently varying T_d by ± 15 K and β_d by ± 0.5 away from our fiducial values of 46 K and 2.0, respectively. The expected shifts in IRX for different combinations of T_d and β_d can be found in fig. 8 of R. A. A. Bowler et al. (2024). We also indicate the corresponding median shifts in the obscured SFRs in Fig. 6. Our assumption of a single-temperature modified blackbody for the FIR dust SED can also bias L_{IR} measurements, as discussed in detail in L. Sommovigo and H. Algera (2025).

Nevertheless, the average attenuation curve slope obtained from the independent methods of fitting directly to the NIRSpec spectra (R. Fisher et al. 2025) and using the IRX–β_{UV} relation are consistent, suggesting that a stellar attenuation curve between the Calzetti-like and SMC relations is most appropriate for the REBELS galaxies. We therefore assume the attenuation curves of R. Fisher et al. (2025) for dust correcting our SFRs in the following sections.

5 STAR FORMATION RATES AND THE STAR-FORMING MAIN SEQUENCE

With these methods to measure dust-obscured star formation, we now compare the SFRs of the REBELS-IFU galaxies inferred using different tracers. We define the SFRs listed in Table 3 as follows:

(i) SFR_{UV} - derived from the rest-UV luminosity of the observed NIRSpec spectra at rest-frame 1500 Å using a top-hat filter of width 100 Å, uncorrected for dust attenuation.

(ii) $SFR_{UV,\,intrinsic\,SED}$ - derived from the reconstructed intrinsic (dust-free) SED model (i.e. corrected for dust attenuation using the curves derived from fits to the NIRSpec spectra in R. Fisher et al. 2025) at rest-frame 1500 Å using a top-hat filter of width 100 Å.

(iii) $SFR_{H\alpha}$ - derived from the H α emission-line flux, corrected for dust attenuation using the Balmer decrement, assuming the attenuation curve derived for each galaxy in R. Fisher et al. (2025).

(iv) SFR_{IR} - dust-obscured SFR derived from the rest-frame FIR ALMA dust continuum detection. We assume a dust temperature of 46 K (R. A. A. Bowler et al. 2024), except for REBELS-25 and REBELS-38, where we use the FIR luminosities presented in H. S. B. Algera et al. (2024a, b) derived from multiband ALMA observations.

Table 3. The SFRs derived from different tracers for the 12 REBELS-IFU galaxies at $z \simeq 7$ studied in this work. From left to right, these are the rest-UV SFR derived directly from the spectra with no dust correction, the dust-corrected rest-UV SFR derived from the reconstructed intrinsic SED, the dust-corrected Hα SFR, the FIR SFR inferred from $L_{\rm IR}$, the FIR SFR inferred using the best-fit IRX–$\beta_{\rm UV}$ relation in Fig. 4, the 100 and 10 Myr SFRs obtained from the SED fits with a non-parametric SFH, and the [C II] SFRs calculated using the calibration of I. De Looze et al. (2014) using the [C II] luminosities presented in H. Algera et al. (2026) and Schouws et al. (in preparation). See Section 5 for a full description of each tracer.

ID	$\rm SFR_{UV}$ $\rm M_\odot\ yr^{-1}$	$\rm SFR_{UV,\ intrinsic\ SED}$ $\rm M_\odot\ yr^{-1}$	$\rm SFR_{H\alpha}$ $\rm M_\odot\ yr^{-1}$	$\rm SFR_{IR}$ $\rm M_\odot\ yr^{-1}$	$\rm SFR_{IR,\ IRX}$ $\rm M_\odot\ yr^{-1}$	$\rm SFR_{100\ Myr}$ $\rm M_\odot\ yr^{-1}$	$\rm SFR_{10\ Myr}$ $\rm M_\odot\ yr^{-1}$	$\rm SFR_{[CII]\ 158\ \mu m}$ $\rm M_\odot\ yr^{-1}$
REBELS-05	12.4 ± 0.8	71 ± 9	113 ± 31	35^{+7}_{-7}	44 ± 9	25^{+2}_{-2}	111^{+15}_{-15}	57 ± 7
REBELS-08	17.7 ± 0.5	54 ± 7	120 ± 44	51^{+10}_{-10}	22 ± 4	15^{+2}_{-2}	90^{+11}_{-12}	61 ± 9
REBELS-12	28.2 ± 0.7	68 ± 10	–	51^{+14}_{-14}	60 ± 10	28^{+4}_{-4}	107^{+24}_{-19}	84 ± 34
REBELS-14	26.1 ± 0.9	68 ± 10	–	33^{+8}_{-8}	49 ± 9	19^{+3}_{-2}	103^{+23}_{-16}	30 ± 9
REBELS-15	28.5 ± 0.9	164 ± 3	185 ± 50	< 35	27 ± 5	25^{+2}_{-2}	248^{+18}_{-16}	16 ± 4
REBELS-18	21.8 ± 0.5	71 ± 7	–	43^{+8}_{-8}	60 ± 11	37^{+4}_{-3}	109^{+15}_{-16}	88 ± 7
REBELS-25	12.0 ± 0.5	52 ± 7	–	55^{+54}_{-20}	30 ± 7	11^{+2}_{-2}	90^{+18}_{-17}	130 ± 9
REBELS-29	19.7 ± 0.7	64 ± 9	57 ± 18	31^{+7}_{-7}	26 ± 5	31^{+6}_{-4}	91^{+14}_{-11}	45 ± 8
REBELS-32	9.1 ± 0.7	63 ± 9	92 ± 25	32^{+9}_{-9}	37 ± 9	24^{+4}_{-4}	89^{+20}_{-14}	64 ± 7
REBELS-34	24.9 ± 0.5	38 ± 4	57 ± 33	< 38	10 ± 2	22^{+2}_{-3}	52^{+8}_{-7}	57 ± 16
REBELS-38	19.6 ± 0.9	87 ± 11	161 ± 68	25^{+17}_{-8}	47 ± 10	42^{+8}_{-6}	132^{+25}_{-22}	139 ± 13
REBELS-39	28.2 ± 1.0	73 ± 10	140 ± 36	41^{+9}_{-9}	21 ± 4	22^{+2}_{-2}	110^{+13}_{-10}	65 ± 21

(v) $\rm SFR_{IR,\ IRX}$ - dust-obscured SFR inferred from the observed rest-UV luminosity and the rest-UV continuum slope from the NIRSpec spectra assuming the IRX–$\beta_{\rm UV}$ relation fitted in Fig. 4.

(vi) $\rm SFR_{10\ Myr}$ or $\rm SFR_{100\ Myr}$ - SFR averaged over 10 or 100 Myr, inferred from the non-parametric SFH of the SED model fitted to the NIRSpec spectra (the same SED model from which $\rm SFR_{UV,\ intrinsic\ SED}$ is derived; see R. Fisher et al. 2025, for details of the SED fitting). These SFRs use all the information in the full NIRSpec spectra rather than a limited wavelength range as in the case of the rest-UV/Hα SFRs. These SED fits do not use the low S/N ALMA FIR data, meaning very obscured regions could potentially be unaccounted for (e.g. J. Márquez et al. 2023). However, as discussed in Section 5.3 of R. Fisher et al. (2025), values derived from the SED fits (e.g. A_V) show good consistency with FIR-derived properties, suggesting this is not the case.

(vii) $\rm SFR_{[CII]\ 158\ \mu m}$ - SFR inferred from the FIR [C II] 158 μm emission-line flux, using the starburst calibration from I. De Looze et al. (2014).

5.1 Significant dust-obscured star formation fractions

To demonstrate the importance of dust-obscured star formation in our sources, in Fig. 5 we show the dust-obscured SFR fractions calculated from $f_{\rm obs} = \rm SFR_{IR}/SFR_{UV+IR}$ (where $\rm SFR_{UV+IR} = SFR_{UV} + SFR_{IR}$). We find high obscured fractions, in the range $f_{\rm obs} = 0.56$-0.78, consistent with those previously derived for the REBELS sources from ground-based photometry (P. Dayal et al. 2022; A. Ferrara et al. 2022; H. Inami et al. 2022; L. Sommovigo et al. 2022a; R. A. A. Bowler et al. 2024), with a significant reduction in the stellar mass uncertainties compared to the previous studies. This is consistent with previous results that nearly half of the star formation in massive ($\log(M_\star/\rm M_\odot) > 9$) galaxies at high-redshift ($z \gtrsim 4$) is known to be dust obscured (e.g. R. A. A. Bowler et al. 2018; Y. Fudamoto et al. 2021; H. Inami et al. 2022; S. Schouws et al. 2023; L. Barrufet et al. 2023; R. A. A. Bowler et al. 2024; H. S. B. Algera et al. 2024a). For comparison, we show the $f_{\rm obs}$–$M_\star$ relation derived from a mass-complete sample of galaxies at $0 < z < 2.5$ by K. E. Whitaker et al. (2017). The limited stellar mass range and selection effects of our sample

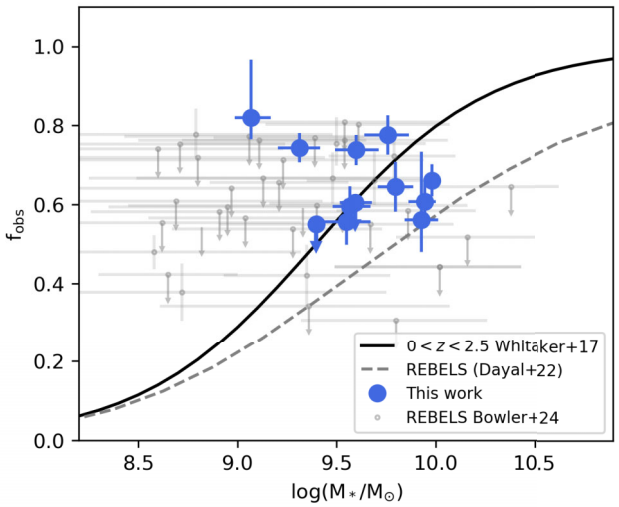

Figure 5. The obscured SFR fractions, $f_{\rm obs} = \rm SFR_{IR}/SFR_{UV+IR}$, versus stellar mass for the 12 REBELS-IFU galaxies at $z \simeq 7$ (blue). The REBELS-IFU galaxies have significant dust-obscured SFR fractions, demonstrating the necessity of robust dust corrections. The small grey points show the obscured fractions for the other REBELS galaxies from R. A. A. Bowler et al. (2024). The $f_{\rm obs}$–$M_\star$ relation derived from a mass-complete sample of galaxies at $0 < z < 2.5$ by K. E. Whitaker et al. (2017) is shown by the black line.

prevent us from ascertaining whether this relation holds at these redshifts; however, the majority of the REBELS-IFU galaxies are approximately consistent with this relation. The four galaxies with the highest $f_{\rm obs}$ values are offset above the K. E. Whitaker et al. (2017) relation. This could reflect intrinsic scatter, or it might suggest that the SED-derived stellar masses are slightly underestimated due to the rest-UV/optical spectra being dominated by the less obscured regions (there is evidence for spatial segregation between the dust and rest-UV emitting regions in these galaxies, see H. Inami et al. 2022). Nevertheless, the high obscured star formation fractions highlight the necessity of robust dust corrections when comparing the total SFRs for our massive sources,

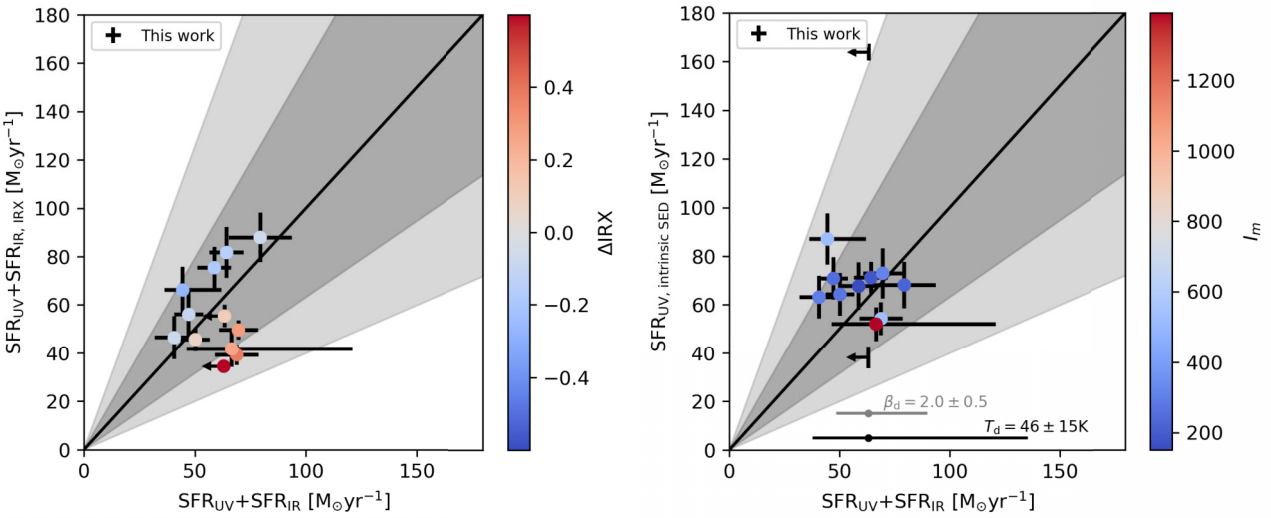

Figure 6. A comparison of two approaches for correcting rest-UV SFRs for dust attenuation. In the left panel, we show the total SFRs derived using the best-fit IRX–β_{UV} relation shown in Fig. 4, SFR$_{UV}$ + SFR$_{IR,\ IRX}$, and in the right panel we show the rest-UV SFRs from the reconstructed intrinsic SED, SFR$_{UV,\ intrinsic\ SED}$. Both methods recover the SFR$_{UV}$+SFR$_{IR}$ values well, with the shaded regions denoting a 0.2 dex and 0.4 dex offset from the 1-to-1 relation. In the left panel, the scatter around the 1-to-1 line corresponds to the offsets of the points from the IRX–β_{UV} relation, as expected. In the right panel, REBELS-15 is an outlier, suggesting dust-age degeneracies in the SED fitting have caused an overestimation of its dust content. On the right, we colour the points by their molecular index, I_m, showing that galaxies with larger I_m values, indicative of a multiphase ISM, tend to be more offset from the 1-to-1 line. The median systematic shift in SFR$_{UV}$+SFR$_{IR}$ with assumed dust temperature, T_d, and dust emissivity index, β_d, are indicated by the black and grey points.

which are more significant than in lower stellar mass sources. We also plot the theoretical predictions based on the REBELS sample from P. Dayal et al. (2022) for comparison, which uses the SFRs calculated in A. Ferrara et al. (2022). The obscured SFR fractions derived from Hα, $f_{obs,\ H\alpha} = 1 - (SFR_{H\alpha,uncorrected}/SFR_{H\alpha})$, are lower due to the wavelength dependence of dust attenuation, but are still significant, ranging between 0.2 and 0.6, demonstrating the need to understand both nebular and continuum dust attenuation (see Section 4).

5.2 Consistency between SFRs derived from the rest-UV

Given the importance of dust-obscured star formation in our sources, in Fig. 6 we test how well SFR$_{UV+IR}$ is recovered by other rest-UV methods. This is also relevant for even higher redshift galaxies, where observations are typically limited to the rest-UV in the absence of less common MIRI observations and FIR detections. In the left panel of Fig. 6, we compare the SFR$_{UV+IR}$ values to those obtained using the IRX–β_{UV} relation fitted in Fig. 4 to correct the unobscured rest-UV SFR. The values show good agreement with SFR$_{UV+IR}$, with the scatter around the 1-to-1 relation corresponding to the offsets of the points from the IRX–β_{UV} curve. This suggests that using the IRX–β_{UV} relation can recover the total SFRs well, although with a strong dependence on the accuracy of the intrinsic UV-slope and attenuation curve slope assumptions.

In the right panel of Fig. 6, we compare the SFR$_{UV,\ intrinsic\ SED}$ values to SFR$_{UV+IR}$. The SFRs derived from the reconstructed dust-free SED models (SFR$_{UV,\ intrinsic\ SED}$) also recover the total SFRs derived from the rest-UV and FIR fluxes (SFR$_{UV+IR}$) well, with a standard deviation around the 1-to-1 relation of 17.6 M$_\odot$ yr^{-1} compared to 17.8 M$_\odot$ yr^{-1} for SFR$_{UV}$ + SFR$_{IR,\ IRX}$. We note that the correlations are actually statistically weak in both cases, although this could be a result of the narrow dynamic range of SFRs we probe. However, REBELS-15 is a strong outlier when using the intrinsic SED method. The FIR dust continuum of REBELS-15 is undetected. Assuming REBELS-15 has a similar dust temperature to the other sources, this suggests that the SED fitting is overestimating the dust attenuation in this source, possibly due to age-dust degeneracies. This demonstrates the limitations of only using the rest-UV/optical emission of a galaxy and the value of multi-wavelength observations, even non-detections. However, we note the possibility that the dust temperature of REBELS-15 could be higher, which would naturally explain the ALMA Band 6 non-detection (e.g. T. J. L. C. Bakx et al. 2020) and simultaneously increase its SFR$_{IR}$. Another effect we must consider that could affect the recovery of the total SFRs is the impact of dust-star geometry. We find that the points with a higher molecular index, $I_m = \frac{F_{158}/F_{1500}}{\beta_{UV}-\beta_{UV,0}}$ (where F_{158} and F_{1500} are the observed continuum flux densities at rest-frame 158 μm and 1500 Å, respectively; see A. Ferrara et al. 2022), tend to deviate more from the 1-to-1 line in the right panel of Fig. 6. Higher I_m values are indicative of the rest-UV and FIR emitting regions being spatially decoupled, suggesting that SED fitting recovers the total SFR less well when galaxies have a more complex, possibly multi-phase ISM. This is also seen in ALPINE galaxies (L. Sommovigo et al. 2022b) and is suggestive of a non-uniform ISM morphology. Future spatially resolved analysis will investigate the effects of these spatial offsets further and their implications for the assumption of energy balance in the SED fitting (Fisher et al., in preparation).

The majority of the SFR$_{[CII]\ 158\ \mu m}$ values show good consistency with the total SFR estimated from SFR$_{UV}$+SFR$_{IR}$. However, we do not discuss the SFRs derived from [C II] further due to the significant uncertainties on the I. De Looze et al. (2014) calibration and ambiguity surrounding where [C II] emission originates from, with some recent studies suggesting it is in fact a better

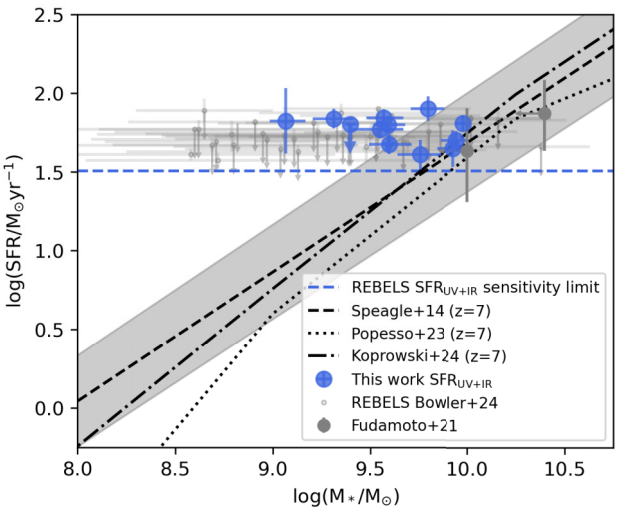

Figure 7. The star-forming main-sequence relation with the 12 massive, $z \simeq 7$ REBELS-IFU galaxies shown in blue. The SFRs are derived by combining the unobscured SFR from the rest-UV and the obscured SFR from the ALMA FIR dust continuum observations (assuming $\beta_d = 2.0$ and $T_d = 46$ K for galaxies without published multiband T_d values). The blue horizontal dashed line shows the SFR threshold of the REBELS survey imposed by the rest-UV bright selection and the sensitivity of the ALMA continuum observations. The small grey points show the other REBELS galaxies (R. A. A. Bowler et al. 2024) and the larger grey points show the serendipitous sources discovered in the REBELS ALMA data (Y. Fudamoto et al. 2021). The REBELS-IFU galaxies lie on or above the main-sequence relations from J. S. Speagle et al. (2014), P. Popesso et al. (2022), and M. P. Koprowski et al. (2024) shown by the dashed, dotted, and dash–dotted lines, respectively. These relations have been extrapolated to $z = 7$ and are derived by combining a range of different tracers.

tracer of neutral atomic gas (H I) or molecular gas (H_2, e.g. K. E. Heintz et al. 2021; D. Vizgan et al. 2022; L. Vallini et al. 2025).

5.3 The star-forming main-sequence with SFR_{UV+IR}

In Fig. 7, we show the total SFRs of the REBELS-IFU galaxies derived by combining the rest-UV and FIR tracers, SFR_{UV+IR}, in comparison to literature star-forming main-sequence relations (assuming $\beta_d = 2.0$ and $T_d = 46$ K, except for REBELS-25 and REBELS-38, for which we use the multi-band T_d values). SFR_{UV+IR} is the most direct way of measuring the total SFR and is independent of dust attenuation curve assumptions. However, it still depends on the assumed luminosity-to-SFR conversion factors and dust temperature. We note that even if we adopt the dust temperatures for these sources presented in A. Ferrara et al. (2022) or L. Sommovigo et al. (2022a), which vary between galaxies, the galaxies still lie systematically above the literature main-sequence relations, and our key results are unaffected. We also caveat that, as discussed at length in L. Sommovigo & H. Algera (2025), assuming a single-temperature modified blackbody for the FIR dust SED can bias L_{IR} measurements. Better sampling of the FIR dust SEDs via multiband ALMA observations is required to place stronger constraints on L_{IR} and thus the dust-obscured SFR. Recently obtained ALMA observations now provide dust continuum detections in two bands for the dust-detected galaxies in this sample (Algera et al. in preparation). Preliminary analysis of these data suggests that we are adopting an appropriate dust temperature and that the SFR_{IR} values remain consistent within the errors, meaning our findings will not significantly change. For the galaxies without published multiband data for which we are assuming $T_d = 46$ K and $\beta_d = 2.0$ we indicate the median systematic shift in SFR_{UV+IR} for variations in dust temperature and dust emissivity index in the right panel of Fig. 6. Although the systematic shifts that could result from variations in these parameters appear large, we highlight that the scatter in our SFR_{UV+IR} values is much smaller than these error bars, suggesting the dust temperatures are not varying this significantly between our sources, and the preliminary analysis of the multi-band data for these sources suggests an average dust temperature consistent with what we assume here (Algera et al. in preparation).

The REBELS-IFU galaxies tend to lie slightly above the star-forming main-sequence relations derived by J. S. Speagle et al. (2014), P. Popesso et al. (2022), and M. P. Koprowski et al. (2024) that have been extrapolated to $z = 7$ (these relations were derived from galaxies up to $z \simeq 6$) and adjusted to match the luminosity-to-SFR conversion factors we use. We also show the other REBELS sources (R. A. A. Bowler et al. 2024) and the serendipitous sources discovered in the ALMA data from the REBELS large program by Y. Fudamoto et al. (2021). The dashed horizontal line shows the approximate SFR threshold of the REBELS survey introduced by the rest-UV bright selection ($M_{UV} \lesssim -21.5$) and the dust continuum sensitivity limits of the ALMA observations. This introduces a bias towards higher SFRs and an artificial flatness in the data points (see also H. S. B. Algera et al. 2022; R. J. Bouwens et al. 2022). The 12 REBELS-IFU sources have some of the brightest [C II] 158 μm detections from the REBELS survey, further biasing this subsample to higher SFRs (e.g. I. De Looze et al. 2014). If we simulate the main sequence using the relation and scatter from J. S. Speagle et al. (2014) and apply the selection cuts, the simulated galaxies occupy a similar region of the parameter space, as indicated by the horizontal line in Fig. 7.

5.4 The star-forming main sequence with other tracers

In Fig. 8, we show the positions of the REBELS-IFU sample with respect to the star-forming main-sequence using other SFR tracers, with tracers that are sensitive to longer (shorter) timescales in the top (bottom) panel. We plot the SFRs derived from the NIRSpec spectra of JADES galaxies in the same redshift range with open circles (D. J. Eisenstein et al. 2025; A. J. Bunker et al. 2024; F. D'Eugenio et al. 2025). The REBELS-IFU galaxies tend to lie above all the main-sequence relations derived using different tracers from CEERS and JADES spectra at $6 < z \leq 7$ by L. Clarke et al. (2024). The forbidden regions set by the maximum SFR averaged over a given timescale as a function of stellar mass that has been formed (see A. C. Carnall et al. 2018) are shown by the shaded regions. For a galaxy to lie in these regions, it would require the SFR averaged over a given timescale to be greater than the total mass formed divided by the total elapsed time.

First we consider the SFR averaged over longer (100 Myr) timescales, comparing $SFR_{UV,\,intrinsic\,SED}$ and $SFR_{100\,Myr}$ (upper panel). While $SFR_{UV,\,intrinsic\,SED}$ shows a flat relation similar to SFR_{UV+IR}, as expected given the relatively good agreement we found between these quantities in Fig. 6, $SFR_{100\,Myr}$ correlates strongly with stellar mass and shows extremely good consistency with the J. S. Speagle et al. (2014) relation and 100 Myr SED-based relation from L. Clarke et al. (2024). As will be discussed further in Section 6.3, $SFR_{UV,\,intrinsic\,SED}$ and SFR_{UV+IR} are calculated using κ values that are derived assuming a constant SFH. This results

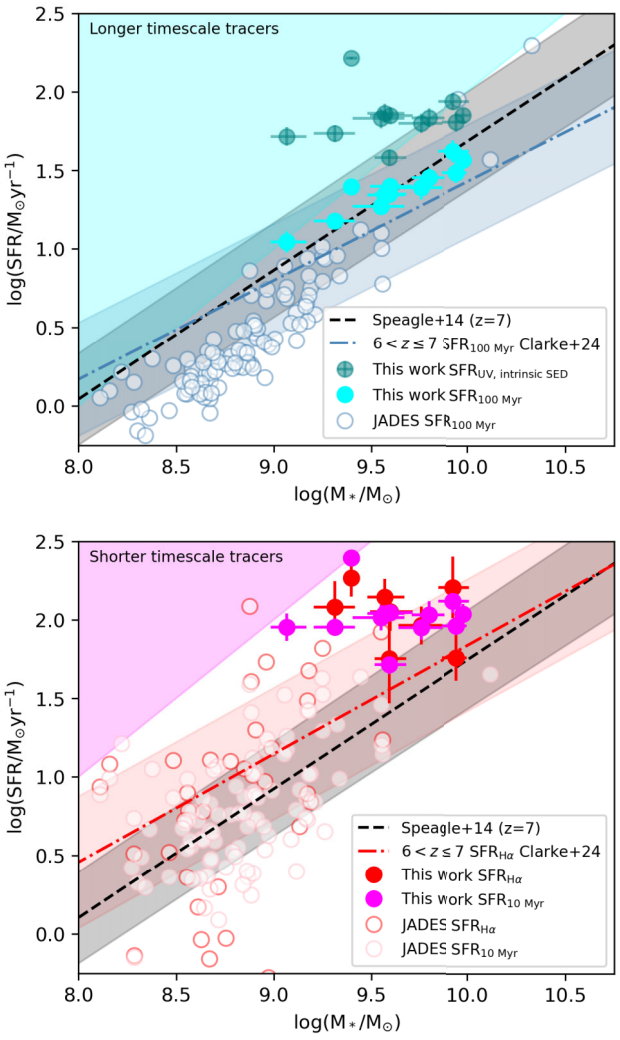

Figure 8. The star-forming main-sequence relation with longer (upper panel) and shorter (lower panel) time-scale tracers. The cyan and magenta shaded areas show the forbidden regions of the parameter space for the 100 and 10 Myr time-scales, derived by assuming all the stellar mass has been formed over that time-scale (A. C. Carnall et al. 2018). In the upper panel, we show that the SFRs derived from the rest-UV flux of the reconstructed intrinsic SEDs, $SFR_{UV,\,intrinsic\,SED}$, in teal and the $SFR_{100\,Myr}$ values (cyan) from the same SED fits. The $SFR_{UV,\,intrinsic\,SED}$ values systematically exceed the $SFR_{100\,Myr}$ values. This discrepancy can be explained by rising SFHs (see Section 6.3). In the bottom panel, we show the $SFR_{H\alpha}$ values in red and the $SFR_{10\,Myr}$ values from SED fitting in magenta. These two tracers agree well. The Hα and 100 Myr main-sequence relations from CEERS and JADES galaxies at $6 < z \leq 7$ are shown by the red and blue dash–dotted lines (L. Clarke et al. 2024), and JADES galaxies in the same redshift range as the REBELS-IFU sample are shown by open circles.

in these tracing the SFR averaged over time-scales shorter than 100 Myr, according to the rising SFHs of the SED fits. Indeed, the majority of the SFR_{UV+IR} and $SFR_{UV,\,intrinsic\,SED}$ values lie in the forbidden region of Fig. 8 and thus cannot be representative of an average SFR over 100 Myr for these SED-derived stellar masses.

Second we consider the SFR averaged over shorter (10 Myr) timescales in the bottom panel, we find good agreement between the $SFR_{10\,Myr}$ and $SFR_{H\alpha}$ values for the eight galaxies in the REBELS-IFU sample at $6.5 \leq z < 7.0$ for which Hα lies within the NIRSpec wavelength coverage. As will be discussed further in Section 6.3, $\kappa_{H\alpha}$ changes less dramatically than κ_{UV} for a rising SFH compared to a constant SFH and thus these continue to trace similar timescales. On average, $SFR_{H\alpha}$ tends to slightly exceed SFR_{UV+IR}, consistent with the rising SFH seen in the SED fits, even though SFR_{UV+IR} and $SFR_{UV,\,intrinsic\,SED}$ are effectively tracing shorter timescales. Similarly, the L. Clarke et al. (2024) main-sequence relation derived using Hα has a higher normalisation and larger scatter than the rest-UV derived relation. The range of $SFR_{H\alpha}$ values in our sample is also slightly larger than SFR_{UV+IR}, but our small sample size makes it challenging to comment on the scatter of the star-forming main-sequence and the implications of this for SFH burstiness. We also note that the REBELS-IFU sources exhibit extended and clumpy morphologies (see L. Komarova et al. 2025; L. E. Rowland et al. 2025) with evidence for spatial offsets between the dust and rest-UV emission (H. Inami et al. 2022; Fisher et al. in preparation). This means that it is possible that SFR differences could be a result of tracers emanating from different regions. The impact of this will be investigated in more detail in upcoming, spatially resolved analysis of these sources (Fisher et al. in preparation; Laza-Ramos et al., in preparation).

6 DISCUSSION

We have derived the SFRs from different tracers for 12 Lyman-break galaxies at $z = 6.5 - 7.7$ using *JWST* NIRSpec spectra and ALMA observations, showing that the majority of these tracers place the REBELS-IFU galaxies above literature $z = 7$ star-forming main-sequence relations. These galaxies have high dust-obscured SFR fractions, but our multiwavelength data allow us to robustly correct for this. We will discuss the physical reasons for discrepancies between SFR tracers and show that the REBELS-IFU SFHs rise more steeply than lower mass galaxies at the same redshift. We illustrate the effects of these rising SFHs on luminosity-to-SFR conversion factors using SED models and present new conversions more relevant for $z \simeq 7$ galaxies. Finally, we use these results to show that the Hα-to-UV luminosity ratio is an unreliable probe of SFH burstiness.

6.1 Tracer time-scales and rising SFHs cause SFR discrepancies

In Fig. 8, we showed the discrepancy between $SFR_{UV,\,intrinsic\,SED}$, derived using the luminosity-to-SFR conversion factor given in Table 2, and the $SFR_{100\,Myr}$ values derived from the same SED fits. The offset between these is greater for the galaxies with more steeply rising SFHs (i.e. it anticorrelates with the mass-weighted ages of the SED fits, such that the discrepancy is larger for younger ages with lower mass-to-light ratios), as will be discussed in more detail in Section 6.3 In Fig. 9 we show that the inferred 10 Myr averaged SFRs from the SED fitting are systematically higher than SFR_{UV+IR}, consistent with a rising SFH and SFR_{UV+IR} probing timescales longer than 10 Myr. However, the 100 Myr SFR values from the SED fitting are systematically lower than the SFR_{UV+IR} values, which is puzzling as SFR_{UV+IR} is expected to probe this time-scale. This discrepancy is a result of using conversion factors that assume a constant SFH in the previous 100 Myr. As will be shown in more detail in Section 6.3, the κ values needed to convert between, for example, $SFR_{100\,Myr}$ and L_{UV} depend on the exact form of the SFH, especially in the rest-UV (see also Fig. 10 in A. Pallottini et al. 2022).

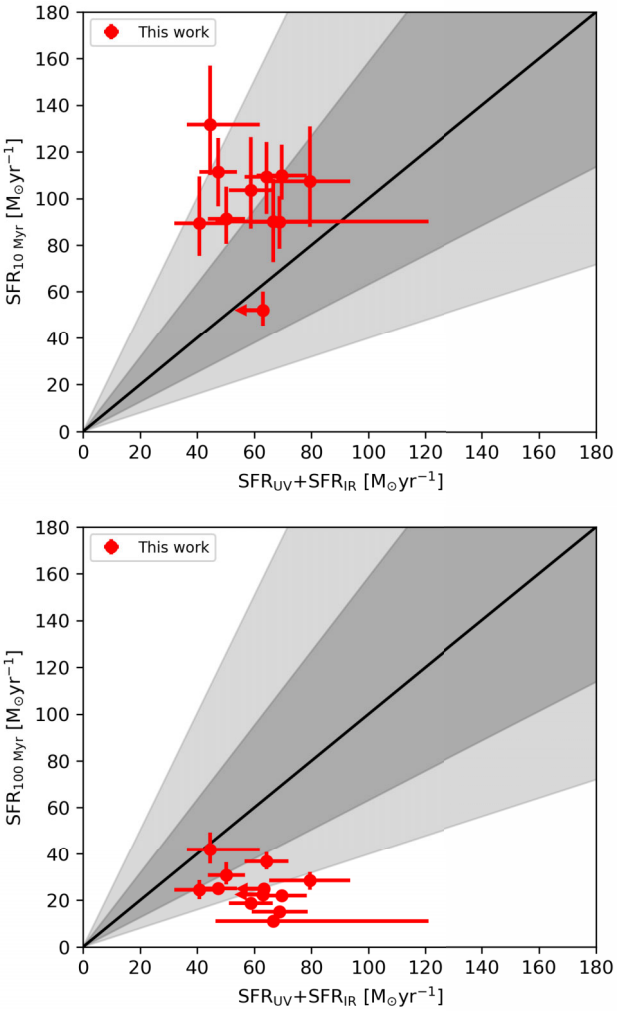

Figure 9. We show that the SFR_{UV+IR} values for the REBELS-IFU galaxies are systematically offset below the SED-derived 10 Myr SFRs (top panel) and above the 100 Myr SFRs (bottom panel). This implies the SFR_{UV+IR} values, calculated using luminosity-to-SFR conversion factors that are derived assuming a constant SFH, are tracing the average SFR over a time-scale between these two values. According to the non-parametric SFHs of our SED fits, our SFR_{UV+IR} values trace the SFR averaged over a median time-scale of $\sim$ 20 Myr.

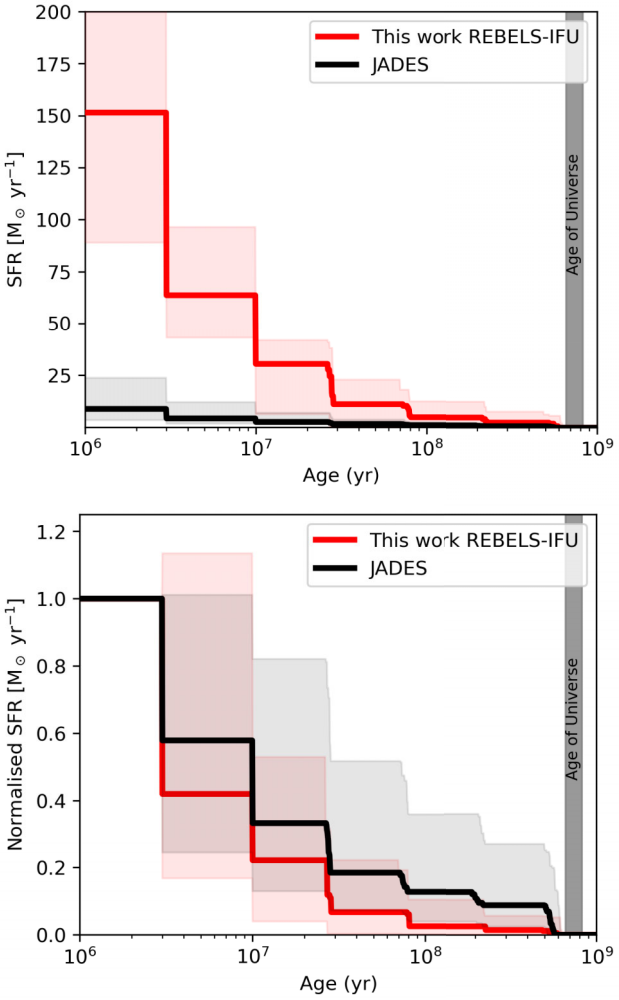

Figure 10. In the top panel, we show the median SFH of the REBELS-IFU galaxies in red. In black, we show the median SFH of JADES galaxies in the same redshift range. The REBELS-IFU SFHs are significantly higher than the JADES galaxies. In the bottom panel, we normalise the SFHs by the most recent bin to compare their shapes and find that the REBELS-IFU SFHs tend to rise more steeply. The shaded regions show the 16th–84th percentile range. The vertical grey bands show the physical cut-off in age set by the age of the Universe at these redshifts.

100 Myr SFRs that are lower than rest-UV derived SFRs have also been found in other observational works. For example, C. A. Pirie et al. (2025) finds dust-corrected SFR_{UV} values that are enhanced by a factor of 2-3 compared to the SED-derived $SFR_{100\,Myr}$ values derived from the NIRCam narrow-band imaging of the JELS (*JWST* Emission Line Survey) galaxies at $z \simeq 6.1$, with the largest offsets in galaxies with lower stellar masses and enhanced recent star formation. We find comparable factors in the REBELS-IFU sample, with SFR_{UV+IR} and $SFR_{UV,\,intrinsic\,SED}$ exceeding $SFR_{100\,Myr}$ by median factors of 2.3 and 2.7, respectively. Thus, there is growing observational evidence that at these redshifts the rest-UV continuum light of galaxies is dominated by fluctuations in star formation on time-scales shorter than 100 Myr, introducing biases in SFRs derived from the rest-UV using κ values that assume constant SFHs. Simulations have also shown that stochastic variability in SFRs can cause rest-UV magnitude variations at these redshifts (e.g. A. Pallottini & A. Ferrara 2023).

These observational results are also consistent with the THESAN-ZOOM hydrodynamics simulations presented in W. McClymont et al. (2025). They find that the 100 Myr SFRs are below the rest-UV SFRs derived using κ values that assume a constant SFH, with the rest-UV SFRs instead probing a time-scale of 24 Myr. If we take the non-parametric SFHs of our SED fits, we find that SFR_{UV+IR} is equivalent to the SFR averaged over a median time-scale of $\sim$ 20 Myr. Similarly, results from the FIRE simulations suggest that, since the integrated rest-UV light of a galaxy is dominated by the young, massive, and short-lived stars, the rest-UV continuum can trace time-scales ranging between 10 Myr and more than 100 Myr, depending on the SFH (J. A. F. Velázquez et al. 2021). This suggests that variability in star formation on time-scales shorter than 100 Myr is introducing scatter and biases into SFRs inferred from the rest-UV emission, introducing scatter to main-sequence relations since the time-scales probed are dependent on the individual galaxy SFH. The

impact of this is likely to increase at higher redshifts, given the evidence that SFHs are more likely to be bursty or rising (e.g. S. Tacchella et al. 2018; J. W. Cole et al. 2025; C. Carvajal-Bohorquez et al. 2025; C. Simmonds et al. 2025), although the simulations of A. Pallottini et al. (2025) suggest SFH stochastity cannot be too high without destroying the observed mass metallicity relation. Thus, SFRs derived from the rest-UV/FIR using calibrations that assume a constant SFH should not be assumed to be equivalent to the 100 Myr average SED result in high-redshift galaxies since they are assuming different SFHs to convert between the observed flux and SFR. The SED-derived SFRs are arguably more informative than the SFR_{UV} or $SFR_{H\alpha}$ values derived in this work since they use all the information in the observed NIRSpec spectra and allow for some flexibility in the SFHs, compared to the very limited wavelength ranges and the (likely invalid) assumptions made to derive the luminosity-to-SFR conversion factors (e.g. constant SFH and fixed metallicity) used for the latter two.

6.2 Star formation histories

To further understand the discrepancies between SFR tracers and the positions of the REBELS-IFU galaxies relative to the main-sequence relations, we investigate their SFHs. SED fits with a constant SFH constrained to have a minimum time-scale of at least 100 Myr fit the spectra poorly. In particular, the lack of a Balmer Break feature in the observed integrated spectra around rest-frame wavelengths of 4000 Å, which is associated with older stars, most notably A-type stars, causes the optical continuum level and emission lines to be poorly fitted (e.g. A. G. Bruzual 1983; B. M. Poggianti & G. Barbaro 1997), suggesting the contribution of these stars to the integrated spectrum is not significant. Our findings are consistent with the work of M. W. Topping et al. (2022) on the REBELS galaxies, which also finds that SED fitting with a constant SFH results in younger ages and masses that are systematically lower than non-parametric fits. On average, our non-parametric masses are 0.35 dex higher than those from the constant SFH, which is similar to the offset of 0.43 dex M. W. Topping et al. (2022) finds. We note that stellar masses derived from integrated spectra can be underestimated compared to pixel-based estimates due to outshining (e.g. C. Giménez-Arteaga et al. 2024). However, these effects are not expected to be significant in high-mass galaxies like these (e.g. N. E. P. Lines et al. 2025).

In Fig. 10, we compare the average non-parametric SFH of the REBELS-IFU galaxies.[1] to the JADES galaxies in the same redshift range[2] We note that the stellar mass distributions of these two samples are not the same, with the median mass of these JADES galaxies being $\log(M_\star/M_\odot) = 8.8$ compared to $\log(M_\star/M_\odot) = 9.6$ for the REBELS-IFU sample. In the top panel of Fig. 10, we find, unsurprisingly, that the median SFH of the REBELS-IFU galaxies is significantly higher than the JADES galaxies. In the bottom panel of Fig. 10, we plot the SFHs normalised by the most recent bin. Although the variation between the galaxies, indicated by the shaded regions, is quite large, the REBELS-IFU SFHs, on average, rise more steeply than the JADES galaxies. Given that lower stellar mass galaxies are generally thought to have more steeply rising or stochastic SFHs (e.g. L. Legrand et al. 2021; T. J. Looser et al. 2025), this is unexpected. However, the bright rest-UV selection bias could go some way to explaining this, with work from the JADES survey by R. Endsley et al. (2024) suggesting that the brightest galaxies in their sample are often experiencing a recent strong upturn in their SFRs. We also note that steeply rising SFHs are consistent with the results of the SERRA simulations presented in M. Kohandel, A. Pallottini & A. Ferrara (2025).

Interestingly, we find that two of the most steeply rising SFHs belong to REBELS-14 and REBELS-39, both of which have two clearly distinct clumps in the IFU imaging (see fig. 1 of L. E. Rowland et al. 2025). This could be evidence for star formation enhancement via merging activity, which results in more steeply rising SFHs (e.g. C. Bottrell et al. 2023, and references therein). Detailed, spatially resolved analysis will investigate this further (Laza-Ramos et al., in preparation), and [C II] kinematic constraints are needed to determine which galaxies in our sample are indeed mergers (Phillips et al., in preparation).

6.3 Simulating the effect of rising SFHs on SFR tracers and κ

Given the strong evidence that our galaxies have non-constant SFRs in the 100 Myr prior to observation, we further investigate the effect of a rising SFH on our results by generating model galaxy SEDs with BAGPIPES (A. C. Carnall et al. 2018, 2019). In Fig. 11, we show a model where we take the fitted SED of a REBELS-IFU galaxy and set the SFH such that the SFR in each time bin in the SFH differs from the previous by a constant ratio. We adjust this bin ratio to create SFHs of varying steepness, keeping all other parameters the same. We also create a model galaxy that has a constant SFH over the same time-scale.

Using the rest-UV and Hα fluxes from the model SEDs, we calculate the κ values required to convert between these luminosities and the known average SFR over 100 or 10 Myr ($SFR_{100\ Myr}$ or $SFR_{10\ Myr}$). These are shown in the top two panels. We see κ_{UV} and $\kappa_{H\alpha}$, which are the ratios between the SFRs and luminosities, both decrease with increasing SFH steepness. This is to be expected because galaxies with more steeply rising SFHs have a greater fraction of their very young, massive stars formed in the more recent past, which dominate the spectra, resulting in greater luminosities for a given time-averaged SED SFR. The fractional decrease in κ_{UV} occurs more rapidly.[3]

In the third row, we show how the $SFR_{H\alpha}/SFR_{UV,\ intrinsic\ SED}$ ratio and the $SFR_{10\ Myr}/SFR_{100\ Myr}$ ratio respond to increasing SFH steepness. $SFR_{H\alpha}$ and $SFR_{UV,\ intrinsic\ SED}$ are calculated using the luminosity-to-SFR conversion factors (κ values) inferred from the constant SFH, consistent with what is commonly assumed in calibrations. Both SFR ratios correlate with steepness, but the

[1]We note that we present the median SFH for the REBELS-IFU sources using the integrated spectra. A detailed analysis of the SFH of each galaxy will be presented in Laza-Ramos et al. in preparation, including spatially resolved component-by-component analysis using the IFU data, which will provide a more comprehensive picture of how these galaxies have built up their stellar mass.

[2]We fit the NIRSpec spectra of the JADES galaxies with the same BAGPIPES set-up as in R. Fisher et al. (2025), except we fix the attenuation curve to D. Calzetti et al. (2000) since we expect their dust content to be lower and thus the attenuation curve slope recovery to be less reliable (see Appendix A of R. Fisher et al. 2025).

[3]We note that in contrast to A. Pallottini et al. (2022), our conversion factor decreases with increasing SFH steepness. This is due to the fact that we calculate κ_{UV} using $SFR_{100\ Myr}$, whereas A. Pallottini et al. (2022) uses the SFR averaged over 20 Myr. Thus, in our case, the rate at which $SFR_{100\ Myr}$ increases is slower than the rate at which L_{UV} increases.

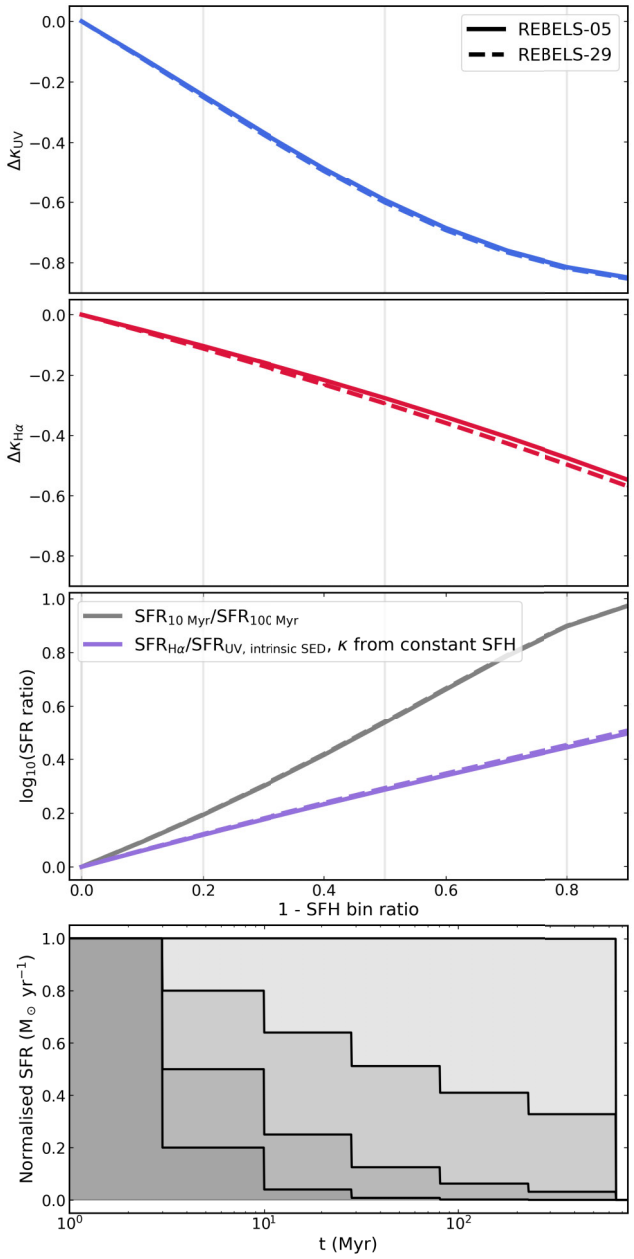

Figure 11. We create model galaxy spectra using BAGPIPES with non-parametric SFHs based on the SED fits to two of the REBELS-IFU galaxies. In the bottom panel, we show the SFHs of increasing steepness, normalised by the most recent SFH bin. The grey vertical lines in the top three panels mark the locations of the constant and three rising SFHs shown. In the top two panels, we show the fractional change in the luminosity-to-SFR conversion factors, κ (calculated using $\kappa_{UV} = SFR_{100\ Myr}/L_{UV}$ and $\kappa_{H\alpha} = SFR_{10\ Myr}/L_{H\alpha}$) compared to the value obtained using a constant SFH against 1− the SFR ratio between succesive time bins in the SFH, i.e. against increasing SFH steepness. The conversion factors both decrease with increasing steepness of the rising SFH, with the variation in κ_{UV} being more significant. In the third row, we show that the $SFR_{10\ Myr}/SFR_{100\ Myr}$ and $SFR_{H\alpha}/SFR_{UV,\ intrinsic\ SED}$ ratios, with the latter assuming the κ values derived from the constant SFH model. These both correlate with the steepness of the SFH, but the $SFR_{H\alpha}/SFR_{UV,\ intrinsic\ SED}$ ratio varies to a lesser degree since the effective time-scales each tracer probes become more closely spaced in time as burstiness increases.

change in the $SFR_{H\alpha}/SFR_{UV,\ intrinsic\ SED}$ ratio is less pronounced than the $SFR_{10\ Myr}/SFR_{100\ Myr}$ ratio. This is driven by the fact that κ_{UV} varies more quickly than $\kappa_{H\alpha}$ and thus the time-scales effectively probed when using κ values from the constant SFH converge. We discuss further in Section 6.5 the implications of this for inferring whether a galaxy has a bursty SFH.

6.4 Deriving new luminosity-to-SFR conversion factors

Given the non-constant nature of the REBELS-IFU SFHs, we derive new luminosity-to-SFR conversion factors from our rising non-parametric SFHs. To convert the observed rest-UV flux, corrected for dust attenuation, to the SFR averaged over 100 Myr inferred from the SED fits ($SFR_{100\ Myr}$) would require a median luminosity-to-SFR conversion factor of

$$\kappa_{UV} = (2.7 \pm 0.9) \times 10^{-29}\ M_\odot\ yr^{-1}\ erg^{-1}\ s\ Hz. \quad (10)$$

To convert the dust-corrected Hα flux to the SFR averaged over 10 Myr inferred from the SED fits ($SFR_{10\ Myr}$) would require a median luminosity-to-SFR conversion factor of

$$\kappa_{H\alpha} = (4.7 \pm 1.4) \times 10^{-42}\ M_\odot\ yr^{-1}\ erg^{-1}\ s. \quad (11)$$

The standard deviations in the κ values are around 30 per cent of the median values, which perhaps should be considered a lower limit on the uncertainty in κ values such as these due to factors such as the variation in the shape of the galaxy SFHs and metallicity. Comparing these to the values in Table 2 that are derived assuming constant SFHs ($\kappa_{UV} = 7.2 \times 10^{-29}\ M_\odot\ yr^{-1}\ erg^{-1}\ s\ Hz$ and $\kappa_{H\alpha} = 4.977 \times 10^{-42}\ M_\odot\ yr^{-1}\ erg^{-1}\ s$), we see that $\kappa_{H\alpha}$ remains approximately consistent, but there is a large systematic shift in κ_{UV} by a factor of $\simeq 2.7$ (> 0.4 dex). Thus, the SFRs derived from the rest-UV with the κ values from a constant SFH would overestimate the 100 Myr SFR by this factor. This has significant implications for deriving SFRs for galaxies at even higher redshifts than our sample, since observations of these sources typically only probe the rest-UV and rising SFHs are increasingly likely (e.g. C. Simmonds et al. 2025). By extension, κ_{IR} will be affected in the same way as κ_{UV}. Therefore, to avoid overestimating the SFR over a given time-scale in galaxies with rising SFHs, adjusted conversion factors like these should be used. We note that the conversion factors applicable to the more abundant lower-mass galaxies at $z \simeq 7$, which, as shown in Fig. 10, may have slightly less steeply rising SFHs, may not be quite as low, and therefore the conversion factors used should be informed by the SFH steepness (see Fig. 11).

6.5 How useful, therefore, are burstiness diagnostics?

Finally, we use our results to assess the usefulness of the ratio of the Hα luminosity, $L_{H\alpha}$, to the monochromatic luminosity at rest-frame wavelength 1600 Å, $\nu L_{\nu,1600}$, as a diagnostic for probing the SFHs of our galaxies.[4] This ratio is commonly used in the literature in both local and high-redshift galaxies to quantify SFH burstiness (e.g. G. R. Meurer et al. 2009; D. R. Weisz et al. 2012; Y. Guo et al. 2016; N. Emami et al. 2019; A. L. Faisst et al. 2019; L. Clarke et al. 2024) with some recent *JWST* studies suggesting

[4]We note that this quantity is closely related to the ionizing photon production efficiency, $\xi_{ion,0}$, presented for this sample in L. Komarova et al. (2025). The values presented there are consistent with what we derive in this work.

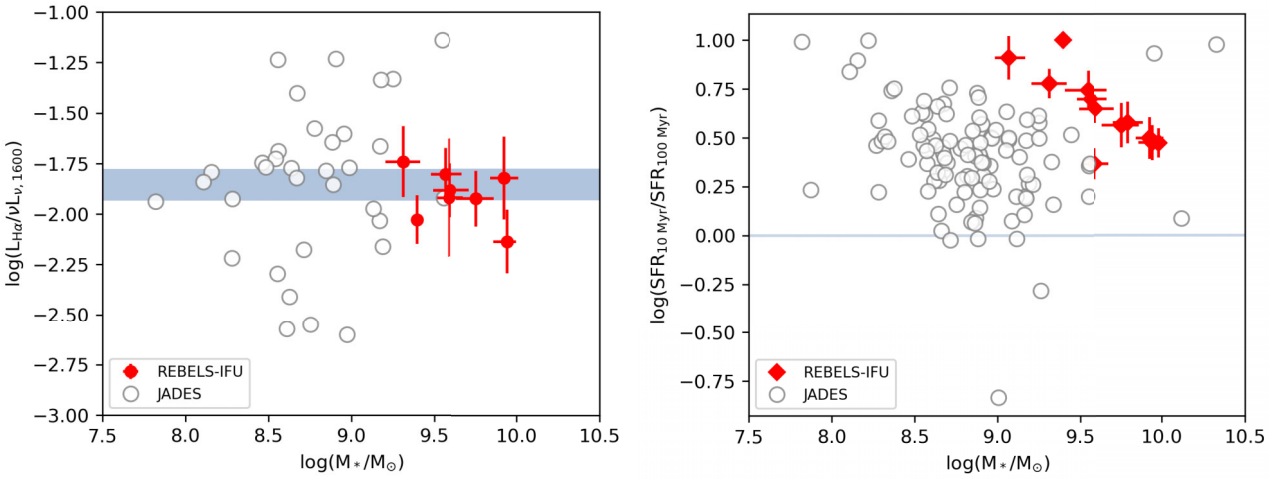

Figure 12. In the left panel, we plot the ratio of the dust-corrected Hα-to-UV luminosities as a function of stellar mass in red for the 8 of the 12 massive galaxies in the REBELS-IFU sample at $6.5 \leq z < 7.0$ for which Hα lies within the NIRSpec wavelength coverage. The ratios are consistent with or below the equilibrium range from V. Mehta et al. (2023) shown by the blue shaded band, which indicates non-bursty SFHs. JADES galaxies at the same redshift as the REBELS-IFU sample are shown as open grey circles. In the right panel, we show that all the REBELS-IFU galaxies have $\log(\mathrm{SFR}_{10\ \mathrm{Myr}}/\mathrm{SFR}_{100\ \mathrm{Myr}}) > 0$, indicative of rising or bursty SFHs, as derived from the SED fitting to the full spectra. This suggests that the Hα-to-UV luminosity ratio can be consistent with non-bursty SFH values even when there is strong evidence for rising SFHs in the 100 Myr prior to observation, implying it cannot reliably identify all bursty SFHs.

lower mass galaxies ($\log(M_\star/\mathrm{M}_\odot) < 9$) with higher emission-line equivalent widths are more bursty (e.g. H. Atek et al. 2022; Y. Asada et al. 2023; C. A. Pirie et al. 2025). In Fig. 12, we show the position of the REBELS-IFU galaxies using the dust-corrected rest-frame UV luminosities.[5] We see that all the REBELS-IFU galaxies are consistent within 1σ errors, or in one case slightly below, the 'equilibrium value' from V. Mehta et al. (2023). These equilibrium values are derived from stellar population synthesis models that suggest the ratio reaches an equilibrium value of -1.93 to -1.78 after 100–200 Myr of constant SFR for the metallicity range $\log(Z/\mathrm{Z}_\odot) = [-2, 0]$. In open grey circles, we show the JADES galaxies at the same redshift range as the REBELS-IFU galaxies. Using this diagnostic ratio, L. Clarke et al. (2024) finds no trend in the burstiness of galaxies with redshift ($1.4 < z < 7$) and suggests that there is a mixture of bursty and non-bursty galaxies at all redshifts.

Whilst M. Sparre et al. (2017) and J. A. F. Velázquez et al. (2021) argue that the Hα to rest-UV flux ratio is a good indicator of star formation burstiness according to the FIRE simulations, other studies, such as S. Rezaee et al. (2023) in typical star-forming galaxies at $z \simeq 2$ from the MOSDEF survey, cast doubt on the reliability of this ratio for probing bursty star formation. Using a spatially resolved analysis of the star formation surface density, stellar population ages, and spectral features in the rest-frame far UV, they find no evidence that elevated Hα-to-UV ratios are indicative of galaxies undergoing bursts of star formation.

The Hα-to-UV flux ratio is conventionally assumed to be a proxy for the 10-to-100 Myr SFR ratio. In the right panel of Fig. 12, we show that the $\mathrm{SFR}_{10\ \mathrm{Myr}}/\mathrm{SFR}_{100\ \mathrm{Myr}}$ ratios are all elevated above the value for a constant SFH and anticorrelate with mass (hinting at a possible mass dependence to the SFH burstiness, although the trend is not obvious in the JADES galaxies). Similarly, we see that the JADES galaxies are also systematically shifted upwards when using this ratio. This is consistent with our model results shown in Fig. 11. Thus, we show that the Hα-to-rest-UV ratio can be consistent with non-bursty values even when there is strong evidence for rapidly rising SFHs over the previous 100 Myr (see Section 6.2). This can also be seen in the simulations of Y. Asada et al. (2023) and V. Mehta et al. (2023). Thus, we conclude that the Hα-to-UV ratio is not a completely reliable probe of burstiness and, at best, only provides a lower limit on how many galaxies are bursty (e.g. L. Clarke et al. 2024). While some studies (e.g. R. Endsley et al. 2025; V. Kokorev et al. 2025) define bursty galaxies as those with $\log(\mathrm{SFR}_{10\ \mathrm{Myr}}/\mathrm{SFR}_{100\ \mathrm{Myr}}) > 0$, C. Carvajal-Bohorquez et al. (2025) suggests only galaxies with values greater than $\gtrsim 0.2$ should be considered bursty. Even with this more stringent constraint, the REBELS-IFU galaxies would be classified as bursty. In addition to the problems introduced by SFH variations, we note that observed Hα-to-rest-UV ratios are highly dependent on dust attenuation correction assumptions, since both the numerator and denominator require correction, and that the Hα-to-UV ratio predicted for a constant SFH is influenced by whether binary stellar evolution is included in the models and the choice of IMF (see S. Rezaee et al. 2023). Therefore, we suggest that SED fitting is likely to be a more reliable method of identifying bursty SFHs, including tests such as inspecting whether features in the galaxy spectra can be reproduced with constant SFHs. We also note that we have not considered shorter time-scale (stochastic) fluctuations in SFHs. This is beyond the scope of this work, but we note that stochastic fluctuations superimposed on a rising SFH (e.g. M. Kohandel et al. 2025) would be hard to distinguish from a steeply rising SFH.

[5]We use the rest-UV flux derived from the intrinsic SED model over that derived from $\mathrm{SFR}_{\mathrm{UV+IR}}/\kappa_{\mathrm{UV}}$ since the ratios using the latter are only available for 6 galaxies by the time we have excluded the four without Hα coverage and the two without ALMA dust continuum detections.

7 CONCLUSIONS

In this work, we present a comprehensive analysis of a range of SFR tracers from a sample of 12 massive Lyman-break galaxies at redshifts $z \simeq 6.5 - 7.7$ known as the REBELS-IFU sample. We derive SFRs from the Hα, rest-UV, and FIR emission and compare these to those obtained from SED fits to the NIRSpec spectra. The main conclusions of this work are:

(i) We find an average stellar-to-nebular attenuation ratio of $f = E(B-V)_{\rm stellar}/E(B-V)_{\rm gas} = 0.50 \pm 0.08$, indicating that differential attenuation remains significant in massive, $z \simeq 7$ galaxies. This ratio is consistent with the $f = 0.44$ factor for local star-forming galaxies (D. Calzetti 1997b), suggesting no clear redshift evolution. However, the large scatter around the average relation implies that nebular attenuation cannot be reliably inferred from the stellar continuum for individual galaxies. We find tentative evidence that the f ratio is metallicity dependent, with the most metal-rich galaxy (REBELS-29) having a ratio consistent with $f = 1$.

(ii) The average attenuation curve inferred from the IRX–$\beta_{\rm UV}$ relation lies between the Calzetti-like and SMC relations, consistent with the attenuation curves derived directly from the NIRSpec rest-UV/optical spectra in R. Fisher et al. (2025). The REBELS-IFU galaxies exhibit high obscured SFR fractions, with $f_{\rm obs} = {\rm SFR_{IR}/SFR_{UV+IR}} = 0.56 - 0.78$, and we utilise the multi-wavelength observations available for our sample to correct the dust-attenuated SFR tracers.

(iii) The REBELS-IFU galaxies lie systematically above literature $z = 7$ star-forming main-sequence relations when using the total SFRs derived from the rest-UV and FIR fluxes ($\rm SFR_{UV+IR}$), the rest-UV SFRs from the reconstructed dust-free intrinsic SED ($\rm SFR_{UV,\,intrinsic\,SED}$), the dust-corrected H$\alpha$ SFRs ($\rm SFR_{H\alpha}$), or the SFRs averaged over a 10 Myr time-scale from the SED fits ($\rm SFR_{10\,Myr}$). However, the SFRs averaged over a 100 Myr time-scale derived from the SED fits ($\rm SFR_{100\,Myr}$) are consistent with literature star-forming main-sequence relations. These discrepancies can be explained with rising SFHs, which causes $\rm SFR_{UV+IR}$ (calculated using the fiducial luminosity-to-SFR conversion factors that are derived assuming a constant SFH) to match the SFR averaged over a time-scale of ~ 20 Myr, not the assumed 100 Myrs. Thus, we demonstrate that it can be misleading to adopt standard SFR conversion factors in high-redshift galaxies that are more likely to have rising or bursty SFHs, especially when comparing $\rm SFR_{UV+IR}$ to $\rm SFR_{100\,Myr}$ or lower-redshift results.

(iv) We find strong evidence for rising SFHs in the REBELS-IFU galaxies when fitting SED models to the integrated spectra. Compared to galaxies from the JADES survey at similar redshifts, the average REBELS-IFU SFH rises more steeply, which is surprising given their high stellar masses, but can be understood considering the rest-UV bright selection of our sample.

(v) Assuming the best-fit non-parametric SFHs for the REBELS-IFU galaxies, we provide new luminosity-to-SFR calibrations more relevant for obtaining the SFRs averaged over 100 Myr of massive $z \simeq 7$ galaxies. We find a median rest-UV luminosity to $\rm SFR_{100\,Myr}$ conversion factor of

$$\kappa_{\rm UV} = (2.7 \pm 0.9) \times 10^{-29}\ {\rm M_\odot\ yr^{-1}\ erg^{-1}\ s\ Hz} \quad (12)$$

and a median Hα luminosity to $\rm SFR_{10\,Myr}$ conversion factor of

$$\kappa_{\rm H\alpha} = (4.7 \pm 1.4) \times 10^{-42}\ {\rm M_\odot\ yr^{-1}\ erg^{-1}\ s}. \quad (13)$$

The spread in these values reflects at least a 30 per cent systematic uncertainty due to factors such as SFH shape and metallicity. The significant systematic decrease in $\kappa_{\rm UV}$ by a factor of $\simeq 3$ (> 0.4 dex) compared to the fiducial value derived assuming a constant SFH is of particular importance for the reliability of SFRs of $z > 12$ objects, where observations typically only probe the rest-UV (since MIRI observations and FIR detections are less commonly available) and SFHs are more likely to be rising. Using model galaxy SEDs from BAGPIPES, we find $\kappa_{\rm UV}$ and $\kappa_{\rm H\alpha}$ both decrease with more steeply rising SFHs, with $\kappa_{\rm UV}$ being more sensitive. Therefore, to avoid overestimating the average SFR over a given time-scale in high-redshift galaxies with rising SFHs, adjusted conversion factors should be used. In Fig. 11, we provide a graph to estimate the shift in conversion factors for a given SFH steepness.

(vi) Despite all the REBELS-IFU galaxies having $\rm SFR_{10\,Myr}/SFR_{100\,Myr} > 1$, indicative of bursty SFHs, the observed Hα-to-UV luminosity ratios for all but one of the galaxies remain consistent (within 1σ) with the non-bursty value. This result is supported by our BAGPIPES model spectra that show the $\rm SFR_{H\alpha}/SFR_{UV}$ ratio varies to a lesser degree than than the $\rm SFR_{10\,Myr}/SFR_{100\,Myr}$ ratio with increasing SFH steepness due to the sensitivity of the rest-UV flux to fluctuations in SFR on time-scales shorter than 100 Myr. This suggests the Hα-to-UV luminosity ratio is not a reliable indicator of bursty SFHs, even with robust dust attenuation corrections.

We have shown that using multiwavelength data provides a more comprehensive picture of the global properties of these galaxies. In future work, we will extend this analysis to spatially resolved scales. This is now possible given the wealth of multiwavelength data we now have for some of these sources – including NIRCam imaging (PID 6480; P.I. Schouws, PID 6036; P.I. Hodge), the NIRSpec IFU spectroscopy, and high-resolution (up to 0.15 arcsec) ALMA Band 6 data for ten of the REBELS-IFU galaxies (see L. E. Rowland et al. 2024, for REBELS-25 and Phillips et al. in preparation and the recently approved ALMA PID: 2025.1.01318.S, P.I. Stefanon). This will further reveal how these galaxies build-up their dust and stellar mass in the first Gyr of the Universe.

ACKNOWLEDGEMENTS

We thank the anonymous referee, whose comments helped to improve this manuscript. We thank the authors of Tsujita et al. (2025) and Faisst et al. (2025) for sharing their ALPINE results with us pre-publication.

RB acknowledges support from an STFC Ernest Rutherford Fellowship [grant number ST/T003596/1]. RKC is grateful for support from the Leverhulme Trust via the Leverhulme Early Career Fellowship.

HSBA gratefully acknowledges support from Academia Sinica through grant AS-PD-1141-M01-2. MA is supported by FONDECYT grant number 1252054, and gratefully acknowledges support from ANID Basal Project FB210003 and ANID MILENIO NCN2024_112. PD warmly acknowledges support from an NSERC discovery grant (RGPIN-2025-06182). JAH acknowledges support from the ERC Consolidator Grant 101088676 ('VOYAJ'). MS acknowledges support from the European Research Commission Consolidator Grant 101088789 (SFEER), from the CIDEGENT/2021/059 grant by Generalitat Valenciana, and from project PID2023-149420NB-I00 funded by MICIU/AEI/10.13039/501100011033 and by ERDF/EU.

This work is based on observations made with the NASA/ESA/CSA *JWST*. The data were obtained from the Mikulski Archive for Space Telescopes at the Space Telescope Science Institute, which is operated by the Association of Universities for Research in Astronomy, Inc., under NASA contract NAS 5–03127 for *JWST*. These observations are associated with programs #1626 and #2659.

DATA AVAILABILITY

The data used in this manuscript will be made available to others upon reasonable request to the authors.

REFERENCES

Ahumada R. et al., 2020, ApJS, 249, 3
Algera H. S. B. et al., 2026, MNRAS, 545, 1897
Algera H. S. B. et al., 2022, MNRAS, 518, 6142
Algera H. S. B. et al., 2024a, MNRAS, 527, 6867
Algera H. S. B. et al., 2024b, MNRAS, 533, 3098
Asada Y. et al., 2023, MNRAS, 527, 11372
Atek H., Furtak L. J., Oesch P., van Dokkum P., Reddy N., Contini T., Illingworth G., Wilkins S., 2022, MNRAS, 511, 4464
Bakx T. J. L. C. et al., 2020, MNRAS, 493, 4294
Barrufet L. et al., 2023, MNRAS, 522, 3926
Barrufet L. et al., 2025, MNRAS, 537, 3453
Battisti A. J. et al., 2022, MNRAS, 513, 4431
Bendo G. J. et al., 2025, MNRAS, 540, 1560
Bottrell C. et al., 2023, MNRAS, 527, 6506
Bouwens R. J. et al., 2012, ApJ, 754, 83
Bouwens R. J. et al., 2022, ApJ, 931, 160
Bowler R. A. A., Bourne N., Dunlop J. S., McLure R. J., McLeod D. J., 2018, MNRAS, 481, 1631
Bowler R. A. A. et al., 2024, MNRAS, 527, 5808
Brinchmann J., Charlot S., White S. D. M., Tremonti C., Kauffmann G., Heckman T., Brinkmann J., 2004, MNRAS, 351, 1151
Bruzual A. G., 1983, ApJ, 273, 105
Bruzual G., Charlot S., 2003, MNRAS, 344, 1000
Bunker A. J. et al., 2023, A&A, 677, A88
Bunker A. J. et al., 2024, A&A, 690, A288
Calzetti D., 1997a, AIP Conference Proceedings, Volume 408, The Ultraviolet Universe at Low and High Redshift. AIP, College Park, MD, p. 403
Calzetti D., 1997b, AJ, 113, 162
Calzetti D., 2012, preprint (arXiv:1208.2997)
Calzetti D., Kinney A. L., Storchi-Bergmann T., 1994, ApJ, 429, 582
Calzetti D., Armus L., Bohlin R. C., Kinney A. L., Koornneef J., Storchi-Bergmann T., 2000, ApJ, 533, 682
Capak P. L. et al., 2015, Nature, 522, 455
Cardelli J. A., Clayton G. C., Mathis J. S., 1989, ApJ, 345, 245
Carnall A. C., McLure R. J., Dunlop J. S., Davé R., 2018, MNRAS, 480, 4379
Carnall A. C. et al., 2019, MNRAS, 490, 417
Carvajal-Bohorquez C. et al., 2025, A&A, 704, A290
Casey C. M., 2012, MNRAS, 425, 3094
Chabrier G., 2003, PASP, 115, 763
Charlot S., Fall S. M., 2000, ApJ, 539, 718
Clarke L., Shapley A. E., Sanders R. L., Topping M. W., Brammer G. B., Bento T., Reddy N. A., Kehoe E., 2024, ApJ, 977, 133
Cochrane R. K. et al., 2021, MNRAS, 503, 2622
Cole J. W. et al., 2025, ApJ, 979, 193
Conroy C., 2013, ARA&A, 51, 393
Conroy C., Gunn J. E., White M., 2009, ApJ, 699, 486
Cullen F., Cirasuolo M., Kewley L. J., McLure R. J., Dunlop J. S., Bowler R. A. A., 2016, MNRAS, 460, 3002
D'Eugenio F. et al., 2025, ApJS, 277, 4
Dayal P. et al., 2022, MNRAS, 512, 989
De Looze I. et al., 2014, A&A, 568, A62
Dunlop J. S. et al., 2017, MNRAS, 466, 861
Eisenstein D. J. et al., 2025, ApJS, 281, 50
Emami N., Siana B., Weisz D. R., Johnson B. D., Ma X., El-Badry K., 2019, ApJ, 881, 71
Endsley R. et al., 2024, MNRAS, 533, 1111
Endsley R., Chisholm J., Stark D. P., Topping M. W., Whitler L., 2025, ApJ, 987, 189
Erb D. K., Shapley A. E., Pettini M., Steidel C. C., Reddy N. A., Adelberger K. L., 2006, ApJ, 644, 813
Faisst A. L., Capak P. L., Emami N., Tacchella S., Larson K. L., 2019, ApJ, 884, 133
Faisst A. L. et al., 2026, ApJS, 282, 19
Fanelli M. N., O'Connell R. W., Thuan T. X., 1988, ApJ, 334, 665
Ferrara A. et al., 2022, MNRAS, 512, 58
Figueira M. et al., 2022, A&A, 667, A29
Fisher R. et al., 2025, MNRAS, 539, 109
Fudamoto Y. et al., 2021, Nature, 597, 489
Fujimoto S. et al., 2025, preprint ()
Giménez-Arteaga C. et al., 2024, A&A, 686, A63
Gordon K. D., Clayton G. C., Misselt K. A., Landolt A. U., Wolff M. J., 2003, ApJ, 594, 279
Guo Y. et al., 2016, ApJ, 833, 37
Hao C.-N., Kennicutt R. C., Johnson B. D., Calzetti D., Dale D. A., Moustakas J., 2011, ApJ, 741, 124
Harikane Y. et al., 2023, ApJS, 265, 5
Heintz K. E., Watson D., Oesch P. A., Narayanan D., Madden S. C., 2021, ApJ, 922, 147
Huo Z., Liu Z., Cui W., Liu C., Liu J., Sun M., Feng S., Li L., 2024, ApJS, 271 15
Inami H. et al., 2022, MNRAS, 515, 3126
Jones G. T., Stanway E. R., 2023, MNRAS, 525, 5720
Kashino D. et al., 2013, ApJ, 777, L8
Kashino D. et al., 2017, ApJ, 835, 88
Katz H. et al., 2022, MNRAS, 518, 592
Kennicutt R. C., 1998, ARA&A, 36, 189
Kennicutt R. C., Evans N. J., 2012, ARA&A, 50, 531
Kohandel M., Pallottini A., Ferrara A., 2025, A&A, 704, A39
Kokorev V. et al., 2025, ApJ, 988, L10
Komarova L. et al., 2025, preprint (arXiv:2511.10743)
Koprowski M. P., Wijesekera J. V., Dunlop J. S., McLeod D. J., owski M. J. M., Lisiecki K., McLure R. J., 2024, A&A, 691, A164
Koyama Y. et al., 2015, MNRAS, 453, 879
Koyama Y., Shimakawa R., Yamamura I., Kodama T., Hayashi M., 2019, PASJ, 71, 8
Kreckel K. et al., 2013, ApJ, 771, 62
Legrand L., Hutter A., Dayal P., Ucci G., Gottlöber S., Yepes G., 2021, MNRAS, 509, 595
Lines N. E. P. et al., 2025, MNRAS, 539, 2685
Liu F.-Y. et al., 2026, MNRAS, 545, 1961
Looser T. J. et al., 2025, A&A, 697, A88
Madau P., Dickinson M., 2014, ARA&A, 52, 415
Álvarez Márquez J. et al., 2023, A&A, 671, A105
McClymont W. et al., 2025, MNRAS, 544, 513
McLure R. J. et al., 2018, MNRAS, 476, 3991
Mehta V. et al., 2023, ApJ, 952, 133
Meurer G. R. et al., 2009, ApJ, 695, 765
Miller J. S., 1974, ApJ, 189, 239
Mitsuhashi I. et al., 2024, ApJ, 971, 161
Moustakas J., Robert C. Kennicutt J., Tremonti C. A., 2006, ApJ, 642, 775
Murphy E. J. et al., 2011, ApJ, 737, 67
Naidu R. P. et al., 2025, preprint (arXiv:2505.11263)
Noeske K. G. et al., 2007, ApJ, 660, L43
Osterbrock D., Ferland G. J., 2006, Astrophysics of Gaseous Nebulae and Active Galactic Nuclei, 2nd. ed. University Science Books, Sausalito, CA
Pallottini A., Ferrara A., 2023, A&A, 677, L4

Pallottini A. et al., 2022, MNRAS, 513, 5621
Pallottini A., Ferrara A., Gallerani S., Sommovigo L., Carniani S., Vallini L., Kohandel M., Venturi G., 2025, A&A, 699, A6
Pannella M. et al., 2015, ApJ, 807, 141
Pirie C. A. et al., 2025, MNRAS, 541, 1348
Planck Collaboration et al.VI, 2020, A&A, 641, A6
Poggianti B. M., Barbaro G., 1997, A&A, 325, 1025
Popesso P. et al., 2022, MNRAS, 519, 1526
Price S. H. et al., 2014, ApJ, 788, 86
Prieto-Jiménez C. et al., 2025, A&A, 701, A31
Puglisi A. et al., 2016, A&A, 586, A83
Reddy N. A., Erb D. K., Pettini M., Steidel C. C., Shapley A. E., 2010, ApJ, 712, 1070
Reddy N. A. et al., 2015, ApJ, 806, 259
Reddy N. A. et al., 2020, ApJ, 902, 123
Rémy-Ruyer A. et al., 2014, A&A, 563, A31
Rezaee S., Reddy N., Shivaei I., Fetherolf T., Emami N., Khostovan A. A., 2021, MNRAS, 506, 3588
Rezaee S. et al., 2023, MNRAS, 526, 1512
Roberts-Borsani G. et al., 2024, ApJ, 976, 193
Rowland L. E. et al., 2024, MNRAS, 535, 2068
Rowland L. E. et al., 2025, preprint (arXiv:2501.10559)
Salim S., Boquien M., Lee J. C., 2018, ApJ, 859, 11
Sanders R. L. et al., 2025, ApJ, 989, 209
Sandles L. et al., 2024, A&A, 691, A305
Santini P. et al., 2017, ApJ, 847, 76
Saxena A. et al., 2024, preprint (arXiv:2411.14532)
Schouws S. et al., 2023, ApJ, 954, 103
Schreiber N. M. F. et al., 2009, ApJ, 706, 1364
Shapley A. E., Sanders R. L., Reddy N. A., Topping M. W., Brammer G. B., 2023, ApJ, 954, 157
Shivaei I. et al., 2015, ApJ, 815, 98
Shivaei I. et al., 2020, ApJ, 899, 117
Simmonds C. et al., 2025, MNRAS, 544, 4551
Smit R., Bouwens R. J., Labbé I., Franx M., Wilkins S. M., Oesch P. A., 2016, ApJ, 833, 254
Smith A. et al., 2022, MNRAS, 517, 1
Sommovigo L., Algera H., 2025, MNRAS, 540, 3693
Sommovigo L., Ferrara A., Pallottini A., Carniani S., Gallerani S., Decataldo D., 2020, MNRAS, 497, 956
Sommovigo L. et al., 2022a, MNRAS, 513, 3122
Sommovigo L. et al., 2022b, MNRAS, 517, 5930
Sparre M., Hayward C. C., Feldmann R., Faucher-Giguère C.-A., Muratov A. L., Kereš D., Hopkins P. F., 2017, MNRAS, 466, 88
Speagle J. S., Steinhardt C. L., Capak P. L., Silverman J. D., 2014, ApJS, 214, 15
Tacchella S. et al., 2018, ApJ, 859, 56
Theios R. L., Steidel C. C., Strom A. L., Rudie G. C., Trainor R. F., Reddy N. A., 2019, ApJ, 871, 128
Topping M. W. et al., 2022, MNRAS, 516, 975
Topping M. W. et al., 2025a, ApJ, 980, 225
Topping M. W. et al., 2025b, MNRAS, 541, 1707
Tsujita A. et al., 2025, preprint (arXiv:2510.18248)
Valentino F. et al., 2015, ApJ, 801, 132
Vallini L. et al., 2025, A&A, 700, A117
Velázquez J. A. F. et al., 2021, MNRAS, 501, 4812
Vizgan D. et al., 2022, ApJ, 929, 92
Weisz D. R. et al., 2012, ApJ, 744, 44
Whitaker K. E., van Dokkum P. G., Brammer G., Franx M., 2012, ApJ, 754, L29
Whitaker K. E. et al., 2014, ApJ, 795, 104
Whitaker K. E., Pope A., Cybulski R., Casey C. M., Popping G., Yun M. S., 2017, ApJ, 850, 208
Witstok J., Jones G. C., Maiolino R., Smit R., Schneider R., 2023, MNRAS, 523, 3119
Woodrum C. et al., 2025, preprint (arXiv:2510.00235)
Yanagisawa H. et al., 2024, ApJ, 974, 180
York D. G. et al., 2000, AJ, 120, 1579
Zavala J. A. et al., 2021, ApJ, 909, 165

APPENDIX A: THE EFFECT OF ATTENUATION CURVE ASSUMPTIONS ON NEBULAR-TO-STELLAR ATTENUATION RATIOS

In Fig. A1, we show the colour excesses for the ionised gas, $E(B-V)_{\rm gas}$, derived from the Balmer decrement, compared to the colour excesses for the stellar continuum, $E(B-V)_{\rm stellar}$, with different attenuation curve assumptions. In the left panel, we assume the J. A. Cardelli et al. (1989) extinction curve for $E(B-V)_{\rm gas}$ and the attenuation curves from R. Fisher et al. (2025) for $E(B-V)_{\rm stellar}$. The average ratio is slightly steeper but consistent within the errors with our fiducial fit shown in Fig. 3. In the right panel, we show that assuming the D. Calzetti et al. (2000) attenuation curve for both $E(B-V)_{\rm gas}$ and $E(B-V)_{\rm stellar}$ results in a slightly shallower slope, but it is still consistent within the errors with our fiducial fit. Thus, we conclude that our attenuation curve assumptions do not significantly affect our main results.

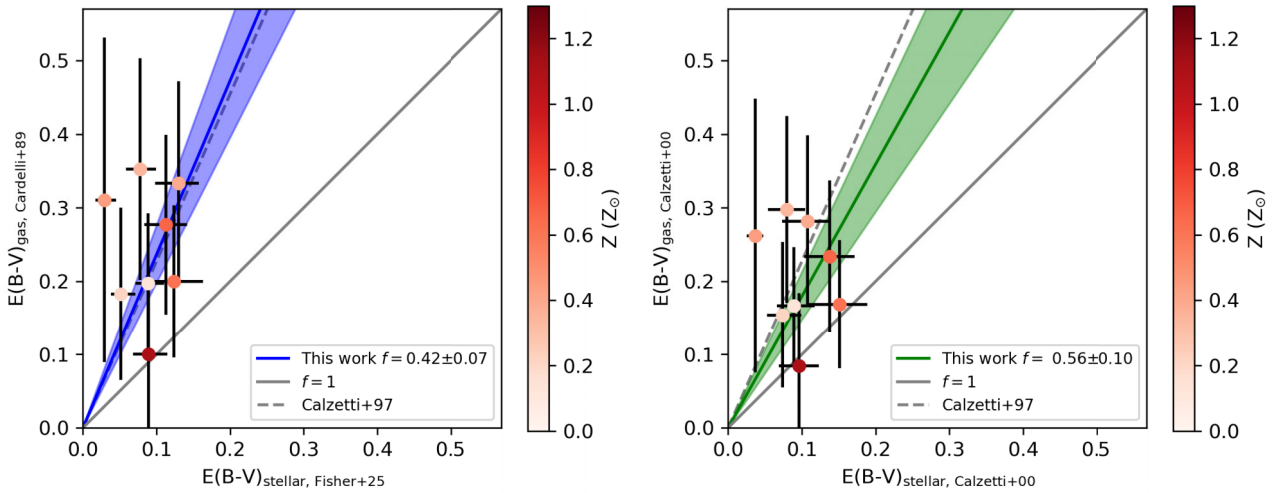

Figure A1. The colour excesses for the ionised gas, $E(B-V)_{\rm gas}$, derived from the Balmer decrement, compared to the colour excesses for the stellar continuum, $E(B-V)_{\rm stellar}$, assuming different attenuation (or extinction) curves. In the left panel, we obtain a slightly steeper gradient when assuming the J. A. Cardelli et al. (1989) extinction curve for $E(B-V)_{\rm gas}$ and the attenuation curves from R. Fisher et al. (2025) for $E(B-V)_{\rm stellar}$. In the right panel, we obtain a slightly shallower gradient when assuming the D. Calzetti et al. (2000) attenuation curve for both $E(B-V)_{\rm gas}$ and $E(B-V)_{\rm stellar}$. However, both gradients are consistent, within the errors, with our fiducial fit shown in Fig. 3.

[1]*Jodrell Bank Centre for Astrophysics, University of Manchester, Oxford Road, Manchester M13 9PL, UK*
[2]*Leiden Observatory, Leiden University, P.O. Box 9513, NL-2300 RA Leiden, the Netherlands*
[3]*Departament d'Astronomia i Astrofisica, Universitat de València, C. Dr Moliner 50, E-46100 Burjassot, València, Spain*
[4]*Unidad Asociada CSIC 'Grupo de Astrofisica Extragaláctica y Cosmología' (Instituto de Fisica de Cantabria – Universitat de València), Spain*
[5]*Institute of Astronomy and Astrophysics, Academia Sinica, 11F of Astronomy-Mathematics Building, No.1, Section 4, Roosevelt Rd, Taipei 106216, Taiwan, R.O.C.*
[6]*Instituto de Estudios Astroficos, Facultad de Ingeniería y Ciencias, Universidad Diego Portales, Av. Ejército 441, Santiago, Chile*
[7]*Millenium Nucleus for Galaxies (MINGAL)*
[8]*International Centre for Radio Astronomy Research, University of Western Australia, 35 Stirling Hwy., Crawley WA 6009, Australia*
[9]*Research School of Astronomy and Astrophysics, Australian National University, Canberra ACT 2611, Australia*
[10]*ARC Centre of Excellence for All Sky Astrophysics in 3 Dimensions (ASTRO 3D), Australia*
[11]*Canadian Institute for Theoretical Astrophysics, 60 St George St, University of Toronto, Toronto ON M5S 3H8, Canada*
[12]*David A. Dunlap Department of Astronomy and Astrophysics, University of Toronto, 50 St George St, Toronto ON M5S 3H4, Canada*
[13]*Department of Physics, 60 St George St, University of Toronto, Toronto ON M5S 3H8, Canada*
[14]*Scuola Normale Superiore, Piazza dei Cavalieri 7, I-56126 Pisa, Italy*
[15]*Hiroshima Astrophysical Science Center, Hiroshima University, 1-3-1 Kagamiyama, Higashi-Hiroshima, Hiroshima 739-8526, Japan*
[16]*Astrophysics Research Institute, Liverpool John Moores University, 146 Brownlow Hill, Liverpool L3 5RF, UK*
[17]*Center for Computational Astrophysics, Flatiron Institute, 162 5th Avenue, New York, NY 10010, USA*
[18]*Department of Astronomy, University of California, 501 Campbell Hall #3411, Berkeley, CA 94720, USA*

This paper has been typeset from a TEX/LATEX file prepared by the author.